Delft University of Technology

Document Version
Final published version

Licence
Dutch Copyright Act (Article 25fa)

Citation (APA)
Gopal, K., Gonugunta, P., Taheri, P., Prem Kumar, D. S., Gnana Prakash, A. P., & Sunitha, D. V. (2026). High efficiency upconversion in PVP passivated $Dy_2O_3$: $Er^{3+}$ nanoparticles enabling solid-state lighting, radiation sensing, forensic security and anti-counterfeiting applications. *Journal of Alloys and Compounds*, *1052*, Article 185961. https://doi.org/10.1016/j.jallcom.2026.185961

Important note
To cite this publication, please use the final published version (if applicable).
Please check the document version above.

Copyright
In case the licence states “Dutch Copyright Act (Article 25fa)”, this publication was made available Green Open Access via the TU Delft Institutional Repository pursuant to Dutch Copyright Act (Article 25fa, the Taverne amendment). This provision does not affect copyright ownership.
Unless copyright is transferred by contract or statute, it remains with the copyright holder.

Sharing and reuse
Other than for strictly personal use, it is not permitted to download, forward or distribute the text or part of it, without the consent of the author(s) and/or copyright holder(s), unless the work is under an open content license such as Creative Commons.

Takedown policy
Please contact us and provide details if you believe this document breaches copyrights.
We will remove access to the work immediately and investigate your claim.

*This work is downloaded from Delft University of Technology.*

Journal of Alloys and Compounds 1052 (2026) 185961

Contents lists available at ScienceDirect

Journal of Alloys and Compounds

journal homepage: www.elsevier.com/locate/jalcom

# High efficiency upconversion in PVP passivated $Dy_2O_3$: $Er^{3+}$ nanoparticles enabling solid-state lighting, radiation sensing, forensic security and anti-counterfeiting applications

Kartik Gopal [a,b], Prasad Gonugunta [c], Peyman Taheri [c], D.S. Prem Kumar [a,b], A.P. Gnana Prakash [d], D.V. Sunitha [a,b,*]

[a] Department of Physics, School of Applied Sciences, REVA University, Bengaluru, Karnataka 560064, India
[b] Center for Advance Materials and Research in Physics, REVA Research Center, REVA University, Bengaluru, Karnataka 560064, India
[c] Department of Materials Science and Engineering (MSE), Delft University of Technology, Delft 2628 CD, the Netherlands
[d] Department of Studies in Physics, University of Mysore, Manasagangotri, Mysore, Karnataka 570220, India

ARTICLE INFO

*Keywords:*
$Dy_2O_3:Er^{3+}$ nanoparticles
PVP Surface passivation
NIR-to-visible upconversion
Solid-state lighting
Anti-counterfeiting inks
Latent fingerprint detection
Trap-engineered thermoluminescence

ABSTRACT

Efficient near-infrared (NIR) to visible upconversion (UC) materials are essential for advancing optoelectronic, radiation sensing, and security devices. In this work, $Dy_2O_3:Er^{3+}$ nanoparticles were synthesized using a solution combustion method and surface-passivated with 9 wt% polyvinylpyrrolidone (PVP) to suppress surface defects and enhance emission efficiency. X-ray diffraction confirmed a cubic phase structure with crystallite size reduced from 22 to 14 nm due to polymer-controlled growth inhibition. Fourier-transform infrared spectra verified PVP coordination with Dy–O and Er–O bonds, while FESEM and HRTEM analyses revealed coral-like nanostructures with a polymer coating (~28 nm average size) and minimized agglomeration. UV–Vis diffuse reflectance spectra indicated bandgap widening from 4.92 to 5.11 eV, consistent with quantum confinement effects. X-ray photoelectron spectroscopy verified stable trivalent $Dy^{3+}$ and $Er^{3+}$ states and formation of an oxygen/nitrogen-rich interface. Under 980 nm excitation, strong UC emissions were observed at 578 nm and 670 nm. The optimized 9 mol% $Er^{3+}$doped sample exhibited an outstanding quantum yield of 84.19 %, a high color rendering index (CRI = 92), and a correlated color temperature (CCT = 5905 K), fulfilling white-light illumination standards. Thermoluminescence measurements under gamma irradiation showed a stable glow peak near 325 °C with trap depths between 0.80–1.17 eV, indicating reliable radiation sensing performance. Demonstrations in latent fingerprint visualization and anti-counterfeiting applications confirm the multifunctionality of the developed material. Overall, PVP-passivated $Dy_2O_3:Er^{3+}$ nanoparticles exhibit superior optical efficiency, structural stability, and functional versatility, establishing them as promising candidates for next-generation optoelectronic, radiation sensing, forensic and security applications

## 1. Introduction

Lanthanide-doped nanoparticles have emerged as a class of materials of significant interest in photonic and optoelectronic technologies owing to their sharp f–f electronic transitions [1–5], long excited-state lifetimes and remarkable photostability. The partial shielding of the 4 f electrons by the filled 5 $s^2 5p^6$ orbitals of rare-earth ions results in narrow emission bands that are minimally affected by the surrounding lattice [6–8], enabling precise spectral tunability across the ultraviolet, visible and near-infrared regions [9–11]. The choice of host lattice plays a pivotal role in determining emission efficiency, energy transfer pathways and device stability [12,13]. Conventional oxide hosts such as yttrium oxide ($Y_2O_3$), gadolinium oxide ($Gd_2O_3$) [14] and lanthanum oxide ($La_2O_3$) have been extensively studied due to their high chemical stability and low phonon energy [15,16]. However, $Y_2O_3$ an efficient upconversion host, can suffer from surface defect–induced quenching at the nanoscale [17]. $Gd_2O_3$ often exhibits high phonon-assisted energy migration losses in heavily doped systems [18]. $La_2O_3$, though optically transparent in the visible range, is hygroscopic, which can limit its long-term stability in ambient environments [19–21]. Among various host matrices,

* Corresponding author at: Department of Physics, School of Applied Sciences, REVA University, Bengaluru, Karnataka 560064, India.
*E-mail address:* sunitha.dv@reva.edu.in (D.V. Sunitha).

https://doi.org/10.1016/j.jallcom.2026.185961
Received 6 November 2025; Received in revised form 24 December 2025; Accepted 3 January 2026
Available online 5 January 2026
0925-8388/© 2026 Elsevier B.V. All rights are reserved, including those for text and data mining, AI training, and similar technologies.

dysprosium oxide ($Dy_2O_3$) has gained attention as a robust platform due to its high thermal and chemical stability, low phonon energy and wide bandgap, which collectively reduces non-radiative losses and favours efficient luminescence processes [22–27].

Erbium ($Er^{3+}$) stands out among lanthanide activators for its rich energy-level structure, which supports both visible upconversion and near-infrared emissions [28–31]. The $^4I_{13/2} \rightarrow {}^4I_{15/2}$ transition at ~1.54 μm is the benchmark for optical telecommunications, while higher-energy transitions enable green ($^2H_{11/2}/{}^4S_{3/2} \rightarrow {}^4I_{15/2}$) and red ($^4F_{9/2} \rightarrow {}^4I_{15/2}$) emissions [32–35], facilitating applications in solid-state lighting, three-dimensional displays and anti-counterfeiting technologies [36,37]. When $Er^{3+}$ is introduced into a $Dy_2O_3$ lattice, $Er^{3+}$ can engage in energy transfer interactions with $Dy^{3+}$, enabling tailored chromaticity and white-light generation. Such multifunctional emission behaviour makes $Er^{3+}$ doped $Dy_2O_3$ as an attractive material for advanced photonic devices, radiation dosimetry and optical security [38–42]. Visible-to-NIR upconversion emission offers a versatile optical response that spans both the human-visible range and biologically transparent NIR region [43–46]. This dual-band emission is valuable for applications such as solid-state lighting, high-density optical data storage and NIR bioimaging [47–49], where deep tissue penetration and reduced background autofluorescence are essential [50,51]. In addition, the NIR component is highly attractive for secure optical communication systems, requiring covert and long-range transmission [52,53]. Despite the potential of $Er^{3+}$ activated $Dy_2O_3$ systems, challenges remain in producing nanoparticles with uniform morphology, homogeneous dopant distribution and minimized surface defects. Conventional synthesis methods often require extended processing times or high annealing temperatures, leading to particle agglomeration and defect-related quenching [54–56]. The relatively new solution combustion synthesis method, leveraging the redox reaction between metal nitrates and organic fuels such as urea, offers a rapid, scalable, and energy-efficient pathway to crystalline rare-earth oxide nanoparticles [57,58]. The inherently exothermic nature of the reaction not only promotes phase formation at relatively low external heating but also yields products with high porosity and large specific surface areas which are favorable for optical activation.

However, as-prepared nanoparticles typically possess a high density of surface states, which serve as a non-radiative recombination centers and diminish emission efficiency. Surface passivation is therefore critical for optimizing photonic performance. Polyvinylpyrrolidone (PVP) has been widely employed for this purpose due to its strong coordination with rare-earth oxide surfaces, ability to suppress quenching sites, and role in improving dispersibility in both aqueous and organic media. In addition to enhancing luminescence efficiency, PVP functionalization can extend the practical usability of nanoparticles in device fabrication, biological imaging and forensic applications.

In recent years, significant progress has been made in the synthesis and optical tailoring of rare-earth–doped upconversion nanomaterials for optoelectronic and sensing applications [59–61]. Modern methods such as microwave-assisted synthesis and solution combustion have enabled better control of particle size, phase purity and luminescence efficiency in $Dy_2O_3$ and related oxide hosts [62,63]. The introduction of polymer passivation such as polyvinylpyrrolidone (PVP) or polyethylene glycol (PEG) improves colloidal stability, minimizes agglomeration and promotes strong coordination on Dy–O and Er–O surface bonds, resulting in superior optical and mechanical robustness [64–66]. Despite these advancements, several challenges remain unresolved: (i) achieving uniform dopant distribution at the nanoscale, (ii) minimizing surface defect–induced quenching under high excitation densities, and (iii) maintaining radiation and photothermal stability under prolonged operation. Moreover, limited studies have focused on correlating polymer–ion interactions with energy-transfer dynamics in $Dy_2O_3$:$Er^{3+}$ matrices. To address these limitations, we report the controlled synthesis of $Er^{3+}$-doped $Dy_2O_3$ nanoparticles via solution combustion route, followed by PVP surface modification to achieve optimal photonic performance. A systematic investigation was carried out over a range of $Er^{3+}$ doping concentrations (1–9 mol%) to elucidate the correlation between composition, structural features and luminescent properties. Furthermore, to identify the optimal activator concentration for enhanced luminescence, the $Er^{3+}$ doping level was systematically varied from 1 to 9 mol%. This approach enabled a detailed evaluation of the correlation between dopant content, structural evolution, and emission efficiency. As concentration increases, the probability of energy transfer upconversion (ETU) between neighboring $Er^{3+}$ ions improve, leading to stronger visible and NIR emissions up to an optimal 9 mol% $Er^{3+}$ content. Beyond this level, typical concentration quenching effects are minimized due to the low phonon energy of the $Dy_2O_3$ host and the defect-suppressing influence of the PVP coating. The identification of this optimal composition ensures maximum photonic output and color stability, laying the foundation for the subsequent sections on luminescence analysis. Comprehensive characterization techniques including powder X-ray diffraction (PXRD), Fourier transform infrared spectroscopy (FTIR), UV–Vis diffuse reflectance spectroscopy (DRS), field emission scanning electron microscopy (FESEM), high-resolution transmission electron microscopy (HRTEM), X-ray photoelectron spectroscopy (XPS), photoluminescence upconversion (PL-UC), and near-infrared photoluminescence (NIR-PL) were employed. The multifunctional applicability of the synthesized nanoparticles was further demonstrated in solid-state white light-emitting diodes (WLEDs), thermoluminescent dosimetry (TLD), anti-counterfeiting inks and latent fingerprint visualization. This work not only addresses the key challenges in the synthesis and surface engineering of rare-earth oxide nanoparticles but also highlights their integration into diverse advanced optoelectronic and forensic applications.

## 2. Experimental methods

### 2.1. Materials

99.99 % pure dysprosium (lll) nitrate hexahydrate ($Dy(NO_3)_3{\cdot}6H_2O$), Erbium (III) nitrate hexahydrate ($Er(NO_3)_3{\cdot}6H_2O$), Urea ($NH_2CO_2NH$), Polyvinylpyrrolidone ($C_6H_9NO$-PVP K-30) and Ethanol ($C_2H_5OH$) were procured from Sigma-Aldrich. The raw materials procured are of analytical grade were used directly for material preparation.

### 2.2. Material synthesis

For the synthesis of erbium-doped dysprosium oxide nanoparticles, stoichiometric amounts of Dysprosium (III) nitrate hexahydrate ($Dy(NO_3)_3{\cdot}6H_2O$, 1.5958 g), Erbium (III) nitrate hexahydrate ($Er(NO_3)_3{\cdot}6H_2O$, 0.0163 g for 1 mol% doping), and urea ($CO(NH_2)_2$, 1.5375 g) were individually weighed and then dissolved collectively in 20 mL of deionized water in a borosilicate beaker. The resulting solution was continuously stirred using a magnetic stirrer set at 400 rpm for 25 min to achieve complete dissolution and homogeneity. Once a clear and uniform precursor solution was obtained, it was transferred into an alumina crucible and placed in a muffle furnace which is preheated to 490 °C. Within minutes, a self-sustaining exothermic redox reaction initiated, facilitated by the urea acting as a fuel. The vigorous release of gaseous byproducts caused the solution to froth, culminating in the rapid formation of a voluminous and porous solid product. After the reaction ceased, the foamy mass was manually scraped out and finely ground using an agate mortar and pestle to yield dry powder. This intermediate powder was then subjected to calcination at 900 °C for 4 h in air atmosphere to enhance crystallinity and remove any residual organic or unreacted species. This procedure resulted in the formation of $Dy_2O_3$ nanoparticles doped with 1 mol% of $Er^{3+}$ ions. The same protocol was systematically applied to synthesize additional doped samples with 3, 5, 7 and 9 mol% $Er^{3+}$ concentrations.

For surface functionalization, a polyvinylpyrrolidone (PVP) passivation was employed to modify the surface of the as-prepared $Dy_2O_3$:$Er^{3+}$

nanoparticles. The PVP concentration was fixed at 9 wt% based on our previous optimization studies, where this ratio provided the best balance between surface coverage and photoluminescence efficiency. Lower concentrations led to incomplete passivation, while higher concentrations introduced excess organic content, quenching the luminescence [67]. For each composition (1–9 mol% $Er^{3+}$), exactly 0.5 g of $Dy_2O_3:Er^{3+}$ nanoparticles were placed into a 50 mL beaker, followed by the addition of 0.045 g of PVP to maintain the 9 wt% ratio. Subsequently, 20 mL of absolute ethanol was introduced into each mixture to serve as the dispersing medium. These dispersions were magnetically stirred at 400 rpm for a duration of 18 h at an ambient temperature to facilitate uniform PVP adsorption onto the nanoparticle surfaces. After completion of the coating process, the colloidal mixtures were dried on a temperature-controlled hot plate maintained at 55 °C for 18 h, allowing complete solvent evaporation and formation of dry PVP-passivated nanoparticles.

### 2.3. Characterization methods

Phase composition and crystallinity were determined using a Rigaku Smart Lab Powder X-ray Diffractometer (CuKα, λ = 1.541 Å, 2θ = 20°–80°, scan rate 2° $min^{-1}$). FTIR spectra were recorded on a Bruker Alpha II spectrophotometer (4000–400 $cm^{-1}$, 0.9 $cm^{-1}$ resolution) in transmission and ATR modes with a KBr beam splitter. Morphology and elemental composition were examined using a VEGA3 TESCAN Field Emission Scanning Electron Microscope (0.2–30 kV) equipped with EDX. Optical absorption (190–3200 nm) was measured using a Thermo Scientific UV–Vis–NIR diffuse reflectance spectrophotometer with a 15 W UV source. Nanoscale imaging and compositional mapping were performed with a Thermo Fisher Talos F200S G2 HRTEM (200 kV, FEG source, 4 K CMOS, in-column EDS). The survey and high-resolution X-ray photoelectron spectra (XPS) were recorded under a vacuum of $10^{-9}$ mbar, at a power of 200 W and accelerating electron voltage of 13.5 kV using a PHI 5400 ESCA system supplied by Physical Electronics Inc. This system is equipped with a non-monochromatic Al Kα radiation (hν = 1486.7 eV). The survey spectrum was recorded with a pass energy of 89.45 eV, whereas the high-resolution spectra were recorded with a pass energy of 71.55 eV. Photoluminescence (PL) studies, including emission, excitation, lifetime, and quantum yield, were conducted on an Edinburgh Instruments FLS1000 spectrometer with a 450 W xenon lamp (250–900 nm) and a 200 mW He–Cd laser (325 nm). Time-resolved PL employed microsecond flash lamps and pulsed laser/LED excitation, with visible (PMT-900) and NIR (PMT-1700) detectors. Thermoluminescence (TL) was measured using a TL1009 Reader (Nucleonix Systems, India) under controlled heating to obtain glow curves for dosimetric analysis. High-resolution imaging for latent fingerprint and anti-counterfeiting demonstrations was carried out using a Canon EOS 80D DSLR camera.

## 3. Result and discussion

### 3.1. Phase analysis

Fig. 1(a) shows the PXRD patterns of $Dy_2O_3$ nanoparticles doped with 1, 3, 5, 7 and 9 mol% $Er^{3+}$ and passivated with 9 wt% PVP, while Fig. 1 (b) presents an enlarged view of the most intense (222) reflection in the 27–31° range. The diffraction peaks at 2θ ≈ 20.34°, 28.96°, 33.61°, 35.62°, 39.78°, 43.11°, 48.18° and 57.24° corresponds to the (211), (222), (400), (411), (323), (501), (440) and (622) planes respectively, which match well with the cubic phase of $Dy_2O_3$ (space group *Ia-3*, JCPDS No. 86–1327) [68]. The absence of impurity peaks confirms the formation of a single-phase structure with complete substitution of $Er^{3+}$ into the $Dy_2O_3$ lattice and no detectable crystalline contribution from the amorphous PVP passivation. A gradual

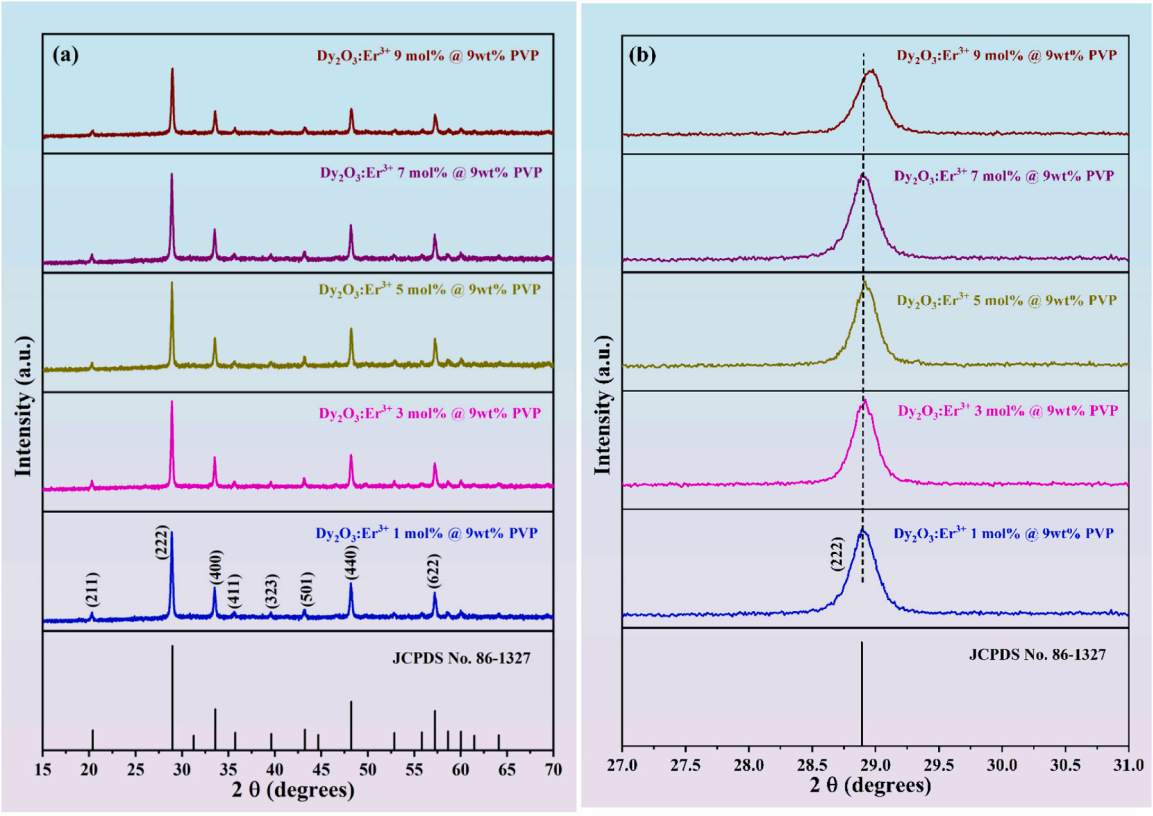


**Fig. 1.** (a) PXRD patterns of $Dy_2O_3:Er^{3+}$ (1–9 mol%) nanoparticles passivated with 9 wt% PVP. (b) Enlarged PXRD patterns in the angle range of 27–31° of $Dy_2O_3:Er^{3+}$ (1–9 mol%) nanoparticles coated with 9 wt% PVP.

broadening and shift of the (222) peak towards higher angles with increasing $Er^{3+}$ concentrations indicates two concurrent effects: (i) lattice contraction due to the replacement of larger $Dy^{3+}$ ions (0.912 Å, CN = 6) with smaller $Er^{3+}$ ions (0.89 Å, CN = 6), consistent with Vegard's law [69], and (ii) reduction in crystallite size caused by dopant-induced lattice strain and the steric hindrance imposed by PVP chains coordinating to surface rare-earth cations.

Debye–Scherrer analysis [70] reveals a systematic decrease in crystallite size from 22 nm (1 mol% $Er^{3+}$) to 14 nm (9 mol% $Er^{3+}$), as summarized in Table 1. This reduction is attributed to strain-induced growth inhibition arising from $Er^{3+}$ substitution and the growth-limiting effect of PVP passivation, which restricts particle coalescence and suppresses crystallite growth during synthesis. The compressive stress generated at the nanoparticle surface during coating further enhances lattice strain, while the polymer passivates surface defects and prevents agglomeration, ensuring uniform dopant dispersion and minimizing concentration quenching. These structural modifications, phase purity, lattice contraction, controlled nanocrystallite size and defect passivation are expected to directly enhance visible and NIR photoluminescence efficiency, improve thermoluminescence sensitivity, and ensure the stability required for multifunctional applications such as solid-state lighting, radiation dosimetry, anti-counterfeiting and latent fingerprint detection.

Fig. 2, shows the FTIR spectra of $Dy_2O_3:Er^{3+}$ (1–9 mol%) nanoparticles passivated with 9 wt% PVP, recorded in the range 4000–400 $cm^{-1}$ . In all samples, the vibrational features correspond to a combination of PVP coating signatures and characteristic Dy–O and Er–O lattice vibrations are clearly visible [71]. A broad absorption band centered at ~3488 $cm^{-1}$ is assigned to the O–H stretching vibrations of physically adsorbed water molecules and surface hydroxyl groups. This is accompanied by weak bands at ~2969 $cm^{-1}$ and ~2876 $cm^{-1}$ , which correspond to asymmetric and symmetric C–H stretching modes of the methylene (–$CH_2$–) groups in the PVP backbone. The peak at ~1658 $cm^{-1}$ is attributed to the C═O stretching vibration of the pyrrolidone ring in PVP. This coordination is a key factor in surface passivation and growth control, as discussed in the PXRD analysis.

Additional PVP-related vibrations are observed at ~1497 $cm^{-1}$ (C–H bending), ~1348 $cm^{-1}$ (C–N stretching coupled with $CH_2$ bending), and ~1289 $cm^{-1}$ (ring deformation modes of the pyrrolidone moiety). The persistence of these peaks across all $Er^{3+}$ concentrations confirm the successful and uniform surface coating of nanoparticles by PVP. In the lower wavenumber region, distinct peaks appear at ~565 $cm^{-1}$ and ~478 $cm^{-1}$ , corresponding to metal–oxygen (Dy–O and Er–O) stretching vibrations in the cubic $Dy_2O_3$ lattice. The presence and intensity of these bands confirm the retention of the oxide phase after PVP coating and dopant incorporation. No additional bands associated with carbonate or other secondary phases are detected, indicating phase purity.

Fig. 3(a) shows the UV–Vis diffuse reflectance spectra (DRS) of $Dy_2O_3$ nanoparticles doped with varying concentrations of $Er^{3+}$ (1–9 mol%) and passivated with 9 wt% PVP. The spectra exhibit multiple absorption

**Table 1**
Estimated crystallite size and band gap values of $Dy_2O_3:Er^{3+}$ (1–9 mol%) nanoparticles passivated with 9 wt% PVP.

| Sample | Average crystallite Size(nm) Debye–Scherrer's method (d) | Band gap (eV) |
|---|---|---|
| $Dy_2O_3$: $Er^{3+}$ 1 mol% @ 9 wt% PVP | 22 | 4.92 |
| $Dy_2O_3$: $Er^{3+}$ 3 mol% @ 9 wt% PVP | 20 | 4.95 |
| $Dy_2O_3$: $Er^{3+}$ 5 mol% @ 9 wt% PVP | 18 | 4.98 |
| $Dy_2O_3$: $Er^{3+}$ 7 mol% @ 9 wt% PVP | 16 | 5.09 |
| $Dy_2O_3$: $Er^{3+}$ 9 mol% @ 9 wt% PVP | 14 | 5.11 |

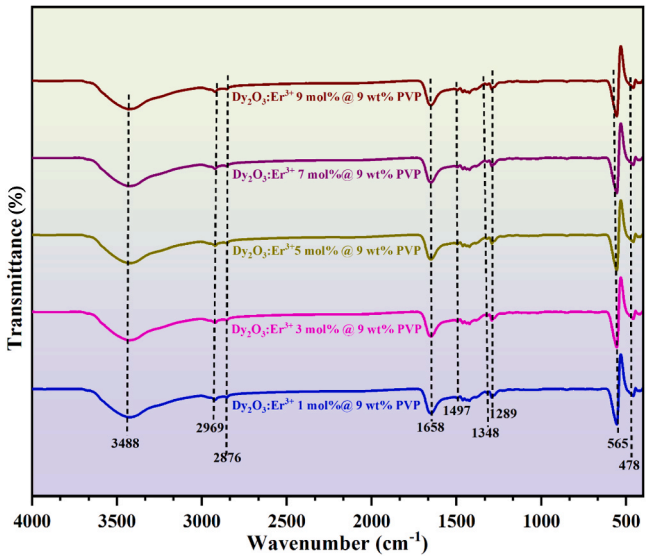


**Fig. 2.** FTIR spectra of $Dy_2O_3:Er^{3+}$ (1–9 mol%) nanoparticles passivated with 9 wt% PVP.

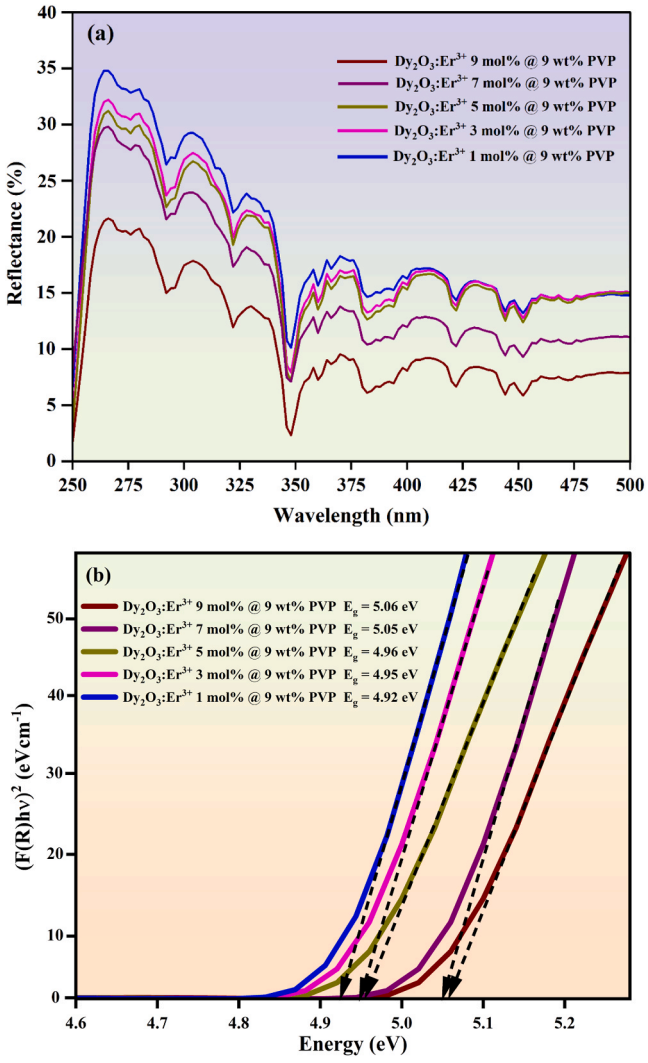


**Fig. 3.** (a) UV-Vis diffuse reflectance spectra and (b) band-gap values of $Dy_2O_3:Er^{3+}$ (1–9 mol%) nanoparticles passivated with 9 wt% PVP.

features in the 250–500 nm range, arising from a combination of host lattice transitions and intra-4f electronic transitions of $Er^{3+}$ ions. The steep absorption edge observed near 250–270 nm is attributed to the intrinsic $O^{2-} \rightarrow Dy^{3+}/Er^{3+}$ charge-transfer transitions in the $Dy_2O_3$ host lattice, while the weaker shoulders and dips between 300–480 nm correspond to characteristic f–f transitions of $Er^{3+}$, which are parity-forbidden but become weakly allowed through vibronic coupling and crystal field perturbations. A systematic decrease in reflectance intensity is observed with increasing $Er^{3+}$ concentration, indicating enhanced photon absorption. This reduction in reflectance due to increased dopant-induced defect states and the influence of the PVP surface coating, improves the light harvesting by minimizing surface scattering and promoting better dispersion. The presence of PVP also reduces surface defect-related backscattering, thus enhancing optical coupling within the nanoparticles.

The optical band gap ($E_g$) values were determined using the Kubelka–Munk function [72] Since the samples exhibits a direct band gap transition, the Tauc relation for direct allowed transitions was employed

$$(F(R)h\nu)2 = A(h\nu - E_g) \quad (1)$$

where $F(R)$ is the Kubelka-Munk function, $h$ is Planck's constant, $\nu$ is the frequency of incident light, $h\nu$ represents the photon energy, $A$ is a proportionality constant, and $E_g$ is the optical band gap energy. The diffuse reflectance ($R$) was first converted into the Kubelka-Munk function using the relation

$$F(R) = \frac{(1-R)^2}{2R} \quad (2)$$

The optical band gap were estimated by plotting $(F(R)h\nu)^2$ against $h\nu$ (Tauc plot) [73] and extrapolating the linear portion to the photon energy axis as illustrated in (Fig. 3(b)). To confirm the nature of the electronic transition, both $(F(R)h\nu)^2$ (direct) and $(F(R)h\nu)^{1/2}$ (indirect) plots were examined. The $(F(R)h\nu)^2$ plots exhibited superior linearity, confirming a direct allowed transition (n = ½) for $Dy_2O_3:Er^{3+}$ nanoparticles. The calculated band gaps of $Dy_2O_3$ nanoparticles doped with varying concentrations of $Er^{3+}$ (1–9 mol%) and coated with 9 wt% PVP increased from 4.92 to 5.06 eV, showing a gradual increase with $Er^{3+}$ content. The calculated band gaps for the samples are listed in Table 1

This band gap widening attributed to the Burstein–Moss effect [74], where substitution of smaller $Er^{3+}$ ions for $Dy^{3+}$ introduces lattice contraction (as confirmed by PXRD), leading to an upward shift of the conduction band edge. Additionally, the reduction in crystallite size with higher doping levels, coupled with surface passivation by PVP, enhances quantum confinement effects, further contributing to the observed blue-shift in the absorption edge. The combined influence of lattice strain, particle size reduction and surface passivation thus accounts for the systematic band gap modulation. From an application standpoint, the ability to tune the optical band gap from 4.92 to 5.06 eV is highly advantageous for optimizing the excitation–emission balance in photoluminescence processes. A wider band gap minimizes unwanted thermal population of higher-energy states, improving the stability of visible and near-infrared emissions under high excitation power. Moreover, reduced reflectance and enhanced absorption in the UV–visible range directly support the efficiency of $Dy_2O_3$ nanoparticles doped with varying concentrations of $Er^{3+}$ coated with 9 wt% PVP in solid-state lighting applications.

### 3.2. Morphology analysis

Fig. 4(a–e) shows the FESEM micrographs of $Dy_2O_3$ nanoparticles doped with 1–9 mol% $Er^{3+}$ ion, each passivated with 9 wt% PVP, (Fig. 4a-d) the particles retain a predominantly granular texture but begin to show denser packing and a slight increase in aggregation. The particle edges appear more defined, suggesting that the dopant modifies nucleation kinetics [75], resulting in tighter clustering of nanocrystallites. At 9 wt% PVP-passivated $Dy_2O_3:Er^{3+}$ 9 mol% (Fig. 4e), the morphology transitions to more compact and coral-like aggregates, composed of fused nanoscale building blocks. This morphological evolution is attributed to dopant-induced strain and localized variations in surface energy, which promote oriented attachment and cluster formation. The PVP coating remains effective in preventing large-scale agglomeration, but the increased dopant content accelerates grain coalescence. The observed morphological changes are consistent with the crystallite size reduction, further supporting the interplay between doping level, surface chemistry and particle growth dynamics.

The corresponding EDX spectra (Fig. 5(a)–e) confirm the elemental composition of the samples. Prominent peaks corresponding to Dy, Er and O are observed in all spectra, verifying the presence of the host lattice and dopant ions. Additional peaks for C and N arise from the PVP coating, which contains pyrrolidone groups. The consistent detection of C and N across all doping levels confirms the uniform surface functionalization achieved by the 9 wt% PVP coating and the elemental composition of samples listed in Table 2. The relative intensity of Er peaks increases systematically with dopant concentration, in agreement with the targeted compositional ratios. No extraneous peaks from impurity elements are detected, indicating high-purity synthesis and successful elimination of unreacted precursors during calcination. This combination of FESEM and EDX results validates that the nanoparticles are composed of $Er^{3+}$-doped $Dy_2O_3$ cores encapsulated by an organic PVP shell (HRTEM confirmed encapsulation of $Er^{3+}$-doped $Dy_2O_3$ nanoparticles, see in the next paragraph) with morphology evolving from porous granular networks to denser aggregates as the dopant concentration increases. Such morphology, combined with controlled surface passivation, is expected to have a significant influence on the optical behavior of the nanoparticles

### 3.3. HRTEM analysis

The HRTEM micrographs of the optimized $Dy_2O_3:Er^{3+}$ (9 mol%) nanoparticles passivated with 9 wt% PVP (Fig. 6. a–b) revealing a nearly spherical morphology with an average particle size of approximately 28 nm, as further confirmed by the particle size distribution histogram in (Fig. 6(e)). In the low-magnification HRTEM images (Fig. 6. a, b), the nanoparticles exhibit a distinct core–shell structure, where the

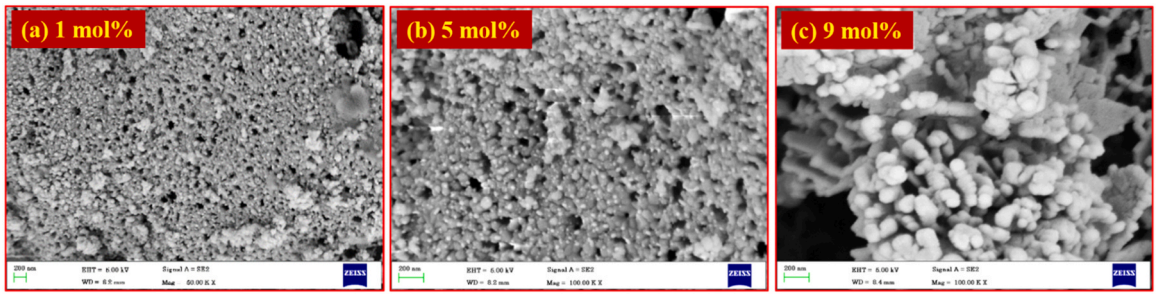


**Fig. 4.** (a-e) FESEM Images of $Dy_2O_3:Er^{3+}$ (1,3 and 9 mol%) nanoparticles passivated with 9 wt% PVP.

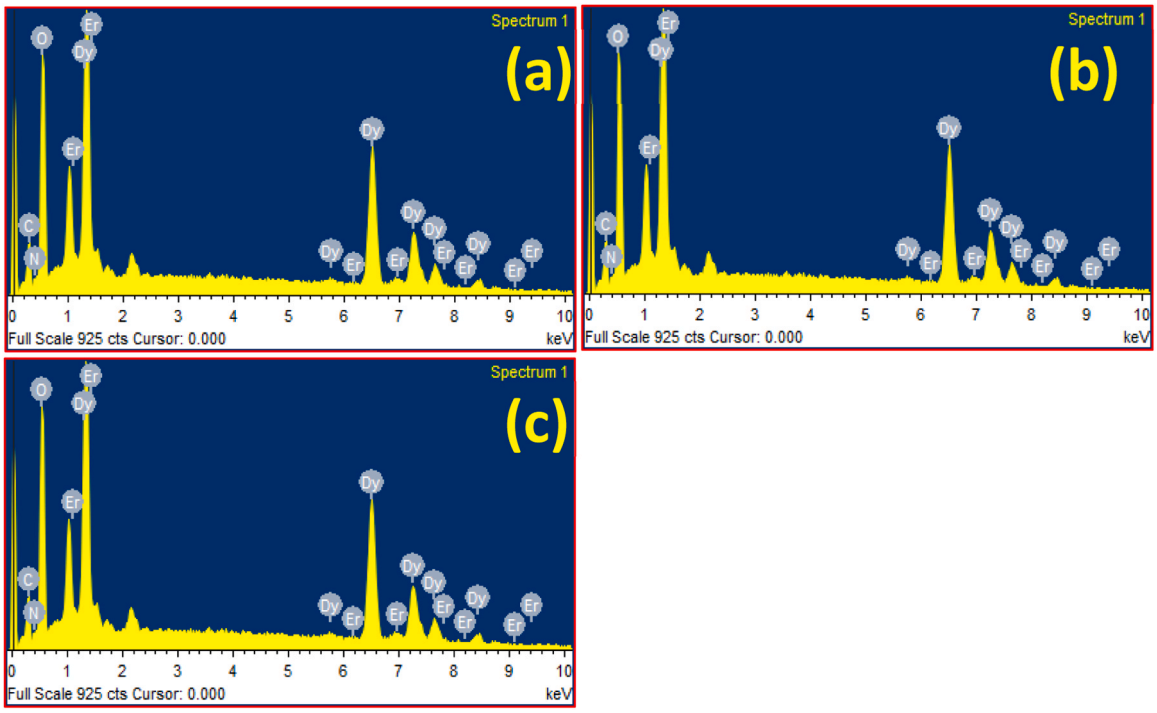


**Fig. 5.** (a-c) EDX Spectra of $Dy_2O_3:Er^{3+}$ (1,3 and 9 mol%) nanoparticles passivated with 9 wt% PVP.

**Table 2**
Elemental composition values of $Dy_2O_3:Er^{3+}$ (1,3 and 9 mol%) nanoparticles passivated with 9 wt% PVP.

| Samples | Elements | Weight % | Atomic % |
|---|---|---|---|
| $Dy_2O_3:Er^{3+}$ 1 mol% @ 9 wt% PVP | C K | 5.27 | 57.90 |
| | N K | 0.71 | 2.69 |
| | O L | 9.06 | 21.41 |
| | Dy L | 82.12 | 16.00 |
| | Er M | 2.84 | 2.00 |
| $Dy_2O_3:Er^{3+}$ 5 mol% @ 9 wt% PVP | C K | 5.15 | 57.10 |
| | N K | 0.78 | 2.80 |
| | O L | 8.95 | 20.60 |
| | Dy L | 71.00 | 15.00 |
| | Er M | 14.12 | 4.50 |
| $Dy_2O_3:Er^{3+}$ 9 mol% @ 9 wt% PVP | C K | 5.05 | 56.70 |
| | N K | 0.82 | 2.90 |
| | O L | 8.85 | 19.90 |
| | Dy L | 59.80 | 12.10 |
| | Er M | 25.48 | 8.40 |

crystalline $Dy_2O_3:Er^{3+}$ core is uniformly encapsulated by an amorphous PVP shell. The PVP layer, clearly visible as a lighter contrast region surrounding the darker crystalline core, provides a uniform thickness and complete coverage, confirming the successful surface functionalization.

This polymer shell serves as a stabilizing barrier, effectively preventing nanoparticle agglomeration and preserving the size distribution obtained from the combustion synthesis stage. The high-resolution lattice imaging (Fig. 6. c) clearly displays well-ordered lattice fringes with an interplanar spacing of 0.318 nm, corresponding to the (2 2 2) planes of cubic $Dy_2O_3$ (JCPDS card No. 86–1327). This observation corroborates the PXRD results and confirms the retention of crystallinity after PVP coating. The uniformity of the fringes across the nanoparticle core indicates minimal lattice distortion, demonstrating that the PVP layer does not disrupt the host lattice structure, while simultaneously protecting it from surface defect formation.

The selected area electron diffraction (SAED) pattern (Fig. 6. d) displays a series of sharp, concentric diffraction rings, indexed to the (2 1 1), (2 2 2), (4 0 0), (4 1 1), (3 2 3), (5 0 1), (4 4 0), and (6 2 2) planes of cubic $Dy_2O_3$. The presence of continuous and well-defined rings, rather than discrete spots, reflects the polycrystalline nature of the nanoparticle ensemble. The intensity and clarity of these rings further confirm high crystallinity, which is critical for efficient upconversion and downconversion luminescence in rare-earth-doped systems. The combined HRTEM and SAED analyses validate the successful incorporation of $Er^{3+}$ ions into the $Dy_2O_3$ host lattice without secondary phase formation, while the homogeneous PVP passivation ensures enhanced stability, controlled growth, and compatibility for targeted optical and forensic applications. The optimized particle morphology, lattice ordering, and surface passivation are expected to synergistically improve optical performance, particularly by minimizing non-radiative pathways and maximizing quantum yield in both visible and NIR regions.

## 4. X-ray photoelectron spectroscopy (XPS) analysis

X-ray photoelectron spectroscopy (XPS) was employed to systematically investigate the surface chemistry and electronic environment [76], of $Dy_2O_3:Er^{3+}$ (9 mol%) nanoparticles before and after encapsulation with 9 wt% polyvinylpyrrolidone (PVP) in order to disentangle the combined effects of $Er^{3+}$ doping and polymer functionalization (Fig. 7.1 a–h). The survey spectrum of the uncoated sample (Fig. 7.1a) showed the presence of expected advantageous carbon (C 1 s) peak, Dy 4d and O 1 s peaks with discernible Er 4d peak, confirming the high purity of the synthesized material. The survey spectrum of the PVP passivated sample (Fig. 7.1b) also showed the presence of expected advantageous carbon/carbon from PVP polymer (C 1 s) peak, Dy 4d and O 1 s peaks with discernible Er 4d peak. In addition, it also showed a minor N 1 s peak which is due to C-N bonds of PVP polymer [77]. High-resolution (HR) C 1 s spectrum of uncoated $Dy_2O_3:Er$ (9 mol%) nanoparticles is shown in Fig. 7.1(c). The sub-peaks at 284.8 and 286 eV are due to C-C and C-O-C of advantageous carbon deposition during XPS measurement. The C 1 s XPS spectrum of PVP passivated $Dy_2O_3:Er$ (9 mol%) nanoparticles (Fig. 7.1d) also showed sub-peaks at 284.7 and 286.1 eV. The peak at 284.7 eV is due C-C bonging of advantageous

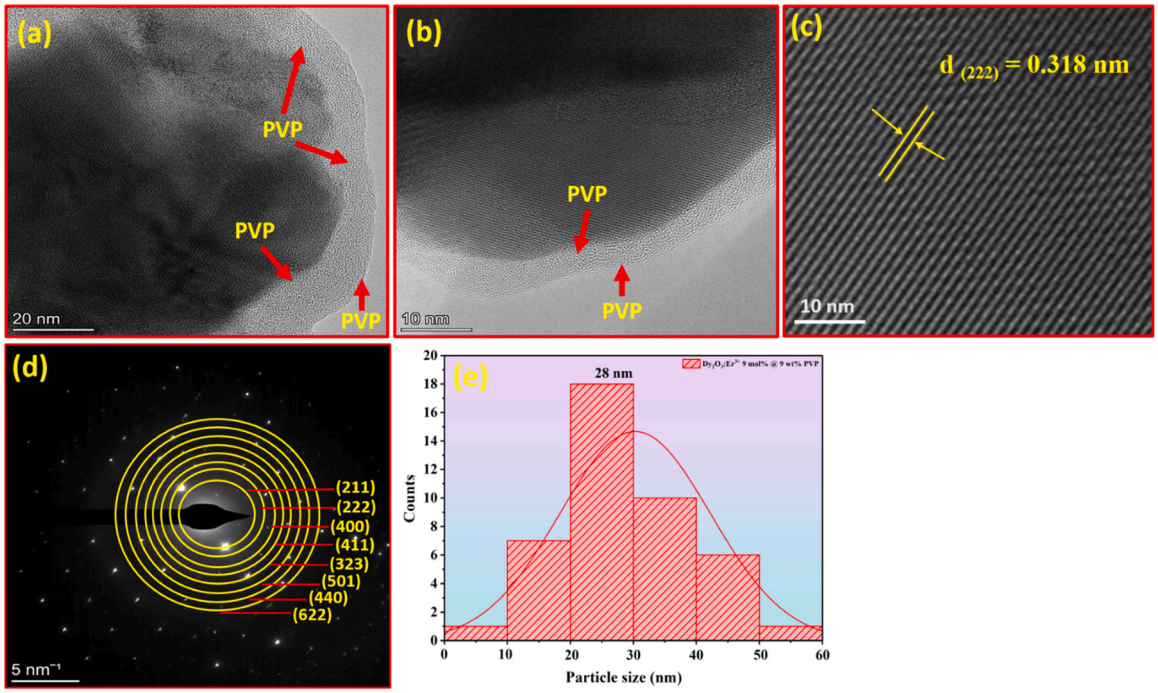


**Fig. 6.** (a-b) HRTEM images of $Dy_2O_3:Er^{3+}$ (9 mol%) nanoparticles passivated with 9 wt% PVP, (c) high-resolution image displaying interplanar spacing, (d) SAED pattern and (d) particle size distribution histogram.

carbon and PVP polymer chain. The sub peak at 286.1 eV is due to C-O-C bonding of advantageous carbon. Here, it is difficult to distinguish advantageous carbon and PVP polymer from C 1 s spectra. High resolution (HR) Dy 4d spectrum of uncoated $Dy_2O_3$:Er (9 mol%) nanoparticles is shown in Fig. 7.1(e). The two sub-peaks at 155.8 and 152.5 eV are due to $4d_{3/2}$ and $4d_{5/2}$, arising from spin orbit coupling of Dy 4d core levels, confirming the presence of trivalent dysprosium [78–80]. The HR Er 4d spectrum is shown in Fig. 7.1(g). The peak at 168.7 eV is due to $Er_2O_3$ [81]. After passivating with 9 wt% PVP, the Dy $4d_{3/2}$ and $4d_{5/2}$ peaks appeared at 152.6 and 152.3 eV (Fig. 7.1f) and Er 4d peak appeared at 168.4 eV (Fig. 7.1h) exhibit a negligible shift compared to spectra of uncoated samples. The minute shift is could be due to PVA passivating around $Dy_2O_2:Er^{3+}$nanoparticles.

The HR O 1 s spectrum of the unpassivation $Dy_2O_2:Er^{3+}$nanoparticles is shown in Fig. 7.2(a). The dominant peak at 529.2 eV arises from lattice oxygen ($O^{2-}$) within $Dy_2O_3$, while the secondary peak at 531.7 eV is assigned to surface hydroxyl groups or adsorbed oxygen species associated with environmental exposure. After PVP passivating (Fig. 7.2b), the O 1 s spectrum with 3 sub-peaks at 529.2, 531.6 and 532.6 eV. The peak at 529.2 eV is due to lattice oxygen ($O^{2-}$) within $Dy_2O_3$. The peak at 532.6 eV became dominant with PVP passivating is due to contribution of C═O bonds in PVP polymer. The appearance of the high-binding-energy peak at 532.6 eV is most likely due to the physisorption of PVP polymer with $Dy_2O_3:Er^{3+}$ surface via carbonyl groups. Perhaps the most decisive evidence of PVP encapsulation is provided by the N 1 s region. The unpassivated $Dy_2O_3:Er^{3+}$ nanoparticles exhibit no nitrogen signal, as expected for a pure oxide material. After PVP passivating (Fig. 7.2d), three distinct peaks emerge at 396.4, 399.5 and 402.9 eV. The peak at 399.5 eV is due to C-N bonds of PVP polymer passivating [76]. The peak at 396.4 eV is likely due to chemisorption of pyrrolidone ring of PVP polymer on $Dy_2O_3:Er^{3+}$ nanoparticles. Safo et al. [82], found that an additional peak in N 1 s XPS spectrum at lower energy when Pt nanocubes coated with PVP. The peak at higher binding energy 402.9 eV is due to chemisorption of PVP via carbonyl group on $Dy_2O_3:Er^{3+}$ nanoparticles in accordance with literature. Xian et al. [83], observed a new sub-peak in N 1 s spectrum at higher energy when PVP is coated palladium (Pd) nanocrystals. Taken together, these HR spectra reveal a coherent mechanistic picture: the $Dy_2O_3:Er^{3+}$ nanoparticles maintain their intrinsic trivalent rare-earth oxidation states upon polymer coating, while the PVP layer binds primarily through its carbonyl oxygen and pyrrolidone nitrogen functionalities, leading to a slight withdrawal of electron density from surface cations and an increase in surface hydroxylation. This interaction stabilizes the nanoparticles, reduces agglomeration, and introduces a tunable interfacial chemistry without compromising the core crystal structure. Such a configuration is ideal for optical and biomedical applications where surface passivation, colloidal stability, and chemical functionality are required, because it maximizes particle stability while preserving the rare-earth electronic structure essential for luminescence or catalytic properties. By combining $Er^{3+}$ doping and PVP passivating, the present work demonstrates a viable route for tailoring the surface and interfacial electronic structure of PVP coated $Dy_2O_3:Er^{3+}$ nanoparticles for advanced applications [84–86].

## 5. Photoluminescence analysis

The photophysical response of $Dy_2O_3:Er^{3+}$ nanoparticles encapsulated in a PVP matrix has been examined under both ultraviolet (UV) and near-infrared (NIR) excitation to elucidate the interplay of down-conversion (DC) and up-conversion (UC) mechanisms. The choice of $Dy_2O_3$ as the host provides a relatively low phonon energy (~450–500 $cm^{-1}$), which minimizes multiphonon relaxation and thereby enhances the probability of radiative 4f–4 f transitions in $Er^{3+}$.

In addition, the presence of $Dy^{3+}$ as a co-dopant influences the population kinetics of $Er^{3+}$ through energy transfer, while the PVP passivation reduces surface-related quenching. Together, these factors yield an optimized luminescent system suitable for photonic applications. The excitation spectrum recorded at 578 nm emission ($^4F_{9/2} \rightarrow {}^6H_{13/2}$) is dominated by a sharp resonance at 352 nm, which is attributed to the $^6H_{15/2} \rightarrow {}^4F_{7/2}$ transition of $Er^{3+}$ (Fig. 8(a)). The large oscillator strength of this band indicates that 352 nm photons efficiently populate higher-lying states, which then feed into lower excited states through rapid non-radiative relaxation. Additional weaker resonances in the 330–440 nm region corresponds to other parity-forbidden f–f

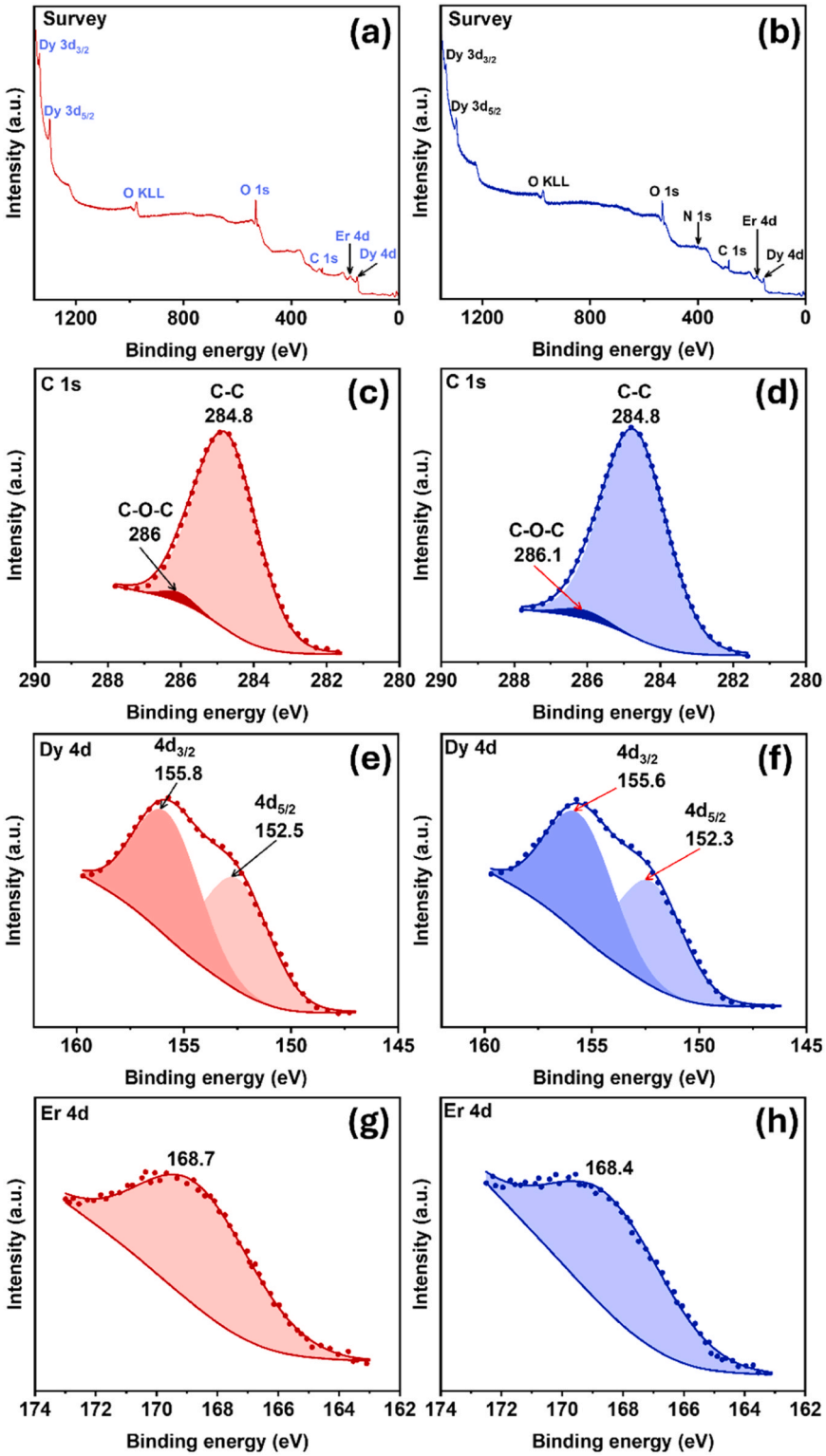


**Fig. 7.1.** Survey spectra of $Dy_2O_3:Er^{3+}$ (9 mol%) nanoparticles before (a) and after 9 wt% PVP passivation (b), HR C 1 s spectra of $Dy_2O_3:Er^{3+}$ (9 mol%) nanoparticles before (c) and after 9 wt% PVP passivation (d), HR Dy 4d 1 s spectra of $Dy_2O_3:Er^{3+}$ (9 mol%) nanoparticles before (e) and after 9 wt% PVP passivated (f). HR Er 4d spectra of $Dy_2O_3:Er^{3+}$ (9 mol%) nanoparticles before (g) and after 9 wt% PVP passivation (h).

transitions, whose narrow linewidths confirm that the local crystal field in $Dy_2O_3$ does not strongly perturb the 4 f orbitals.

Fig. 8(b) shows under 352 nm excitation, the PL emission spectrum exhibits characteristic $Er^{3+}$ multiplets in the violet (~410 nm, $^2H_{9/2} \rightarrow {}^4I_{15/2}$), blue (~490 nm, $^4F_{9/2} \rightarrow {}^6H_{15/2}$), green (~555–580 nm, $^4F_{9/2} \rightarrow {}^6H_{13/2}$), and red (~665 nm, $^4F_{9/2} \rightarrow {}^4I_{15/2}$) regions. The relative intensities of these bands are strongly influenced by the competition between radiative decay and multiphonon relaxation [87,88]. Because $Dy_2O_3$ has a comparatively low phonon cutoff energy, non-radiative relaxation from higher states such as $^2H_{9/2}$ and $^4S_{3/2}$ is suppressed, which enhances the observed green and red emissions. The strong red emission suggests the presence of cross-relaxation processes among $Er^{3+}$

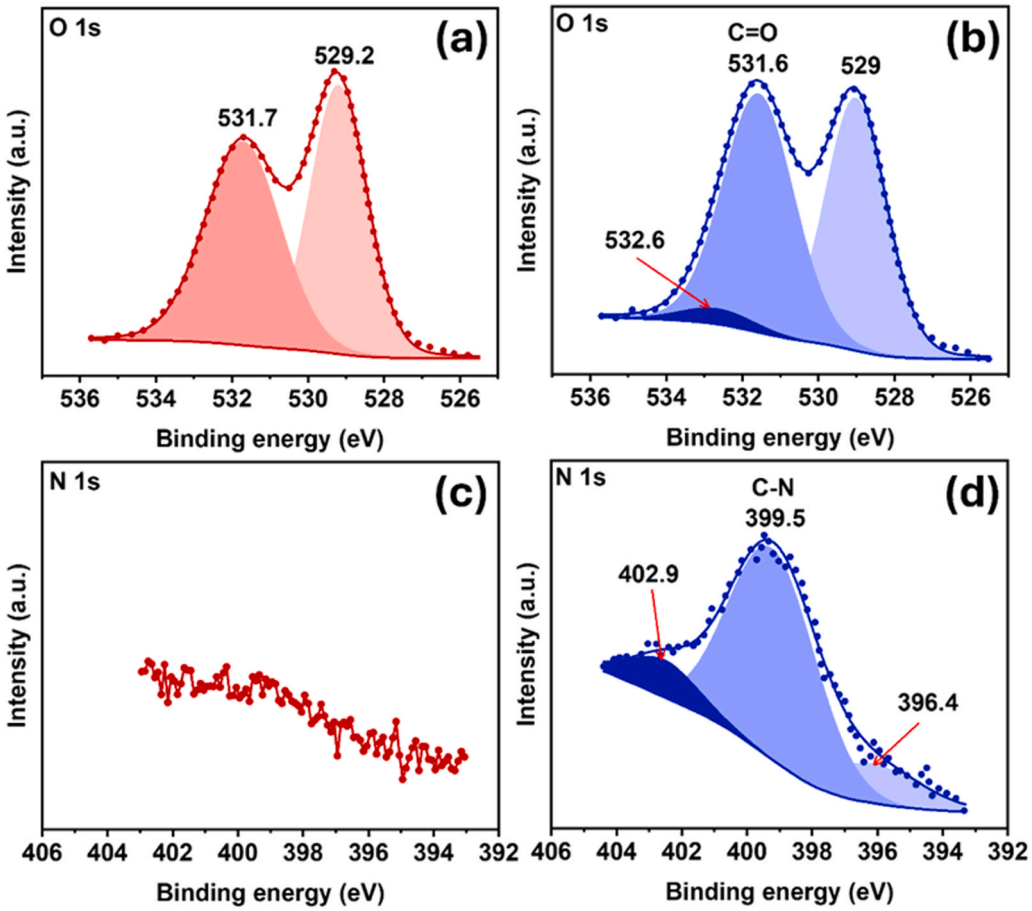


**Fig. 7.2.** High resolution O 1 s spectra of $Dy_2O_3:Er^{3+}$ (9 mol%) nanoparticles before (a) and after 9 wt% PVP coating (b), High resolution N 1 s spectra of $Dy_2O_3:Er^{3+}$ (9 mol%) nanoparticles before (c) and after 9 wt% PVP passivaion (d).

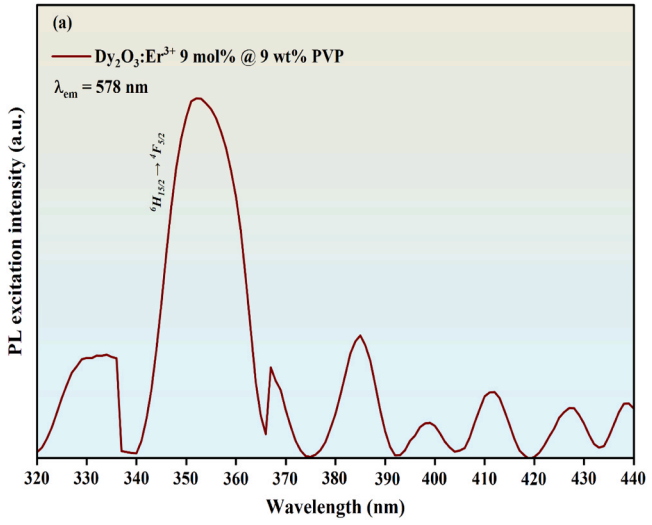


**Fig. 8a.** PL excitation spectra of $Dy_2O_3:Er^{3+}$ 9 mol% passivated with 9 wt% PVP nanoparticles.

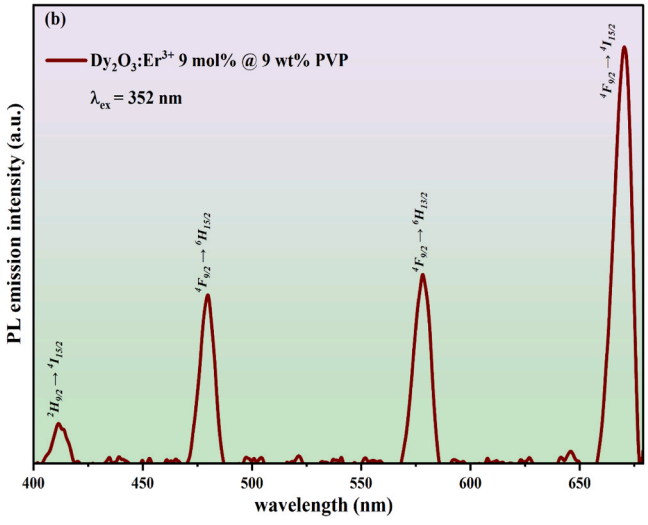


**Fig. 8b.** PL emission spectra of $Dy_2O_3:Er^{3+}$ (9 mol%) passivated with 9 wt% PVP nanoparticles.

ions, in which two adjacent excited ions exchange energy such that one ion relaxes to $^4I_{15/2}$ while the other is promoted to $^4F_{9/2}$, thereby feeding the red channel more efficiently. This is consistent with the known cooperative upconversion and cross-relaxation dynamics of high $Er^{3+}$ concentration systems.

When excited with a 980 nm diode laser, $Dy_2O_3:Er^{3+}$@PVP nanoparticles exhibit pronounced UC emission in the visible region (Fig. 9(a)). The excitation wavelength directly promotes electrons from the $^4I_{15/2}$ ground state to the metastable $^4I_{11/2}$ level. From this reservoir, two sequential processes occur: (i) excited-state absorption (ESA), in which a single ion sequentially absorbs two photons, and (ii) energy transfer up-conversion (ETU), in which a pair of neighboring $Er^{3+}$ ions

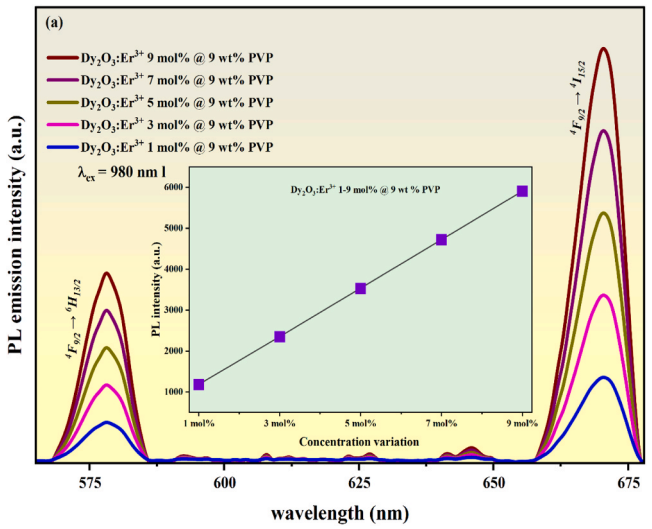


**Fig. 9a.** PL emission spectra recorded at 980 nm Laser diode excitation with $Dy_2O_3:Er^{3+}$ (1–9 mol%) nanoparticles passivated with 9 wt% PVP (inset: Variation of PL intensity with $Er^{3+}$ concentration).

exchange energy, one ion relaxing to the ground state while the other is promoted to a higher level. Both pathways populate the $^4F_{7/2}$, $^2H_{11/2}$, and $^4S_{3/2}$ manifolds, which subsequently relax radiatively, giving rise to the observed green (~555–580 nm) and red (~665–675 nm) bands.

The concentration dependence of the UC intensity (Fig. 9(a), inset) reveals that the emission scales approximately linearly with $Er^{3+}$ concentration up to 9 mol%, reflecting the dominance of ETU processes that rely on interionic interactions. At higher dopant loadings, cross-relaxation processes redistribute population preferentially into the $^4F_{9/2}$ state, which explains the observed enhancement of red emission relative to green. This color-tunability is of particular interest for photonic applications requiring wavelength-selective emission.

Fig. 9(b) shows the emission spectra in the 1400–1600 nm range exhibit intense near-infrared bands. The strongest peak, centered at ~1550 nm, corresponds to the $^4I_{13/2} \rightarrow {}^4I_{15/2}$ transition, with weaker features in the 1440–1490 nm range arising from $^4I_{11/2} \rightarrow {}^4I_{13/2}$ transition. The high intensity of the 1550 nm transition is particularly notable, as it lies within the telecommunication C-band [89], where silica fibers exhibit minimal loss. This indicates that $Dy_2O_3:Er^{3+}$ nanoparticles not only serve as visible light emitters but also as promising gain media for optical communication systems. The observation of strong NIR emission alongside visible UC further highlights the dual-functional nature of this material system.

The efficiency of both DC and UC processes is influenced by the host lattice. $Dy_2O_3$, with its relatively low phonon cutoff, minimizes multi-phonon relaxation and enhances radiative branching ratios. Furthermore, $Dy^{3+}$ ions serve as auxiliary sensitizers, facilitating energy transfer to $Er^{3+}$ and increasing the probability of photon upconversion. The PVP shell reduces surface-related non-radiative recombination pathways by passivating dangling bonds and surface traps, thereby improving luminescence yield. This polymer encapsulation also enhances the dispersion stability of the nanoparticles, which is beneficial for bio-imaging and device integration. The coexistence of DC and UC in $Dy_2O_3:Er^{3+}$@ 9 wt% PVP nanoparticles enables multifunctional applications. The visible DC emission under UV excitation makes them suitable for phosphors in displays and lighting, as well as optical tagging and security printing. The strong NIR-to-visible UC emission provides a basis for bio-imaging, where excitation in the NIR reduces tissue autofluorescence and scattering while visible emission yields high imaging contrast. Simultaneously, the intense 1550 nm emission places this material in direct relevance to optical communication technologies, where it could serve as a gain medium for erbium-doped fiber amplifiers (EDFAs). Moreover, the ability to up-convert sub-bandgap NIR photons into visible photons opens pathways for spectral management in solar energy harvesting, potentially improving the efficiency of silicon-based photovoltaics [90,91].

The observed down-conversion (DC) and up-conversion (UC) processes in $Dy_2O_3:Er^{3+}$ 1–9 mol% coated with 9 wt% PVP nanoparticles energy-level diagram as shown in Fig. 10. Upon excitation with 352 nm radiation, electrons are directly promoted from the ground state $^4I_{15/2}$ to the higher-lying $^4F_{7/2}$ state. This state relaxes non-radiatively to lower-lying manifolds such as $^2H_{9/2}$, $^2H_{11/2}$, $^4S_{3/2}$, and $^4F_{9/2}$, from which characteristic radiative transitions are observed. The violet emission at ~410 nm arises from the $^2H_{9/2} \rightarrow {}^4I_{15/2}$ transition, while the blue band around 490 nm originates from $^4F_{9/2} \rightarrow {}^4I_{15/2}$. The strong green emissions in the 545–580 nm range correspond to the $^2H_{11/2} \rightarrow {}^4I_{15/2}$ and $^4S_{3/2} \rightarrow {}^4I_{15/2}$ transitions, whereas the dominant red band at ~650–670 nm results from the $^4F_{9/2} \rightarrow {}^4I_{15/2}$ transition. These processes confirm the efficient population of intermediate excited states following UV excitation and their subsequent radiative relaxation, giving rise to intense visible DC luminescence.

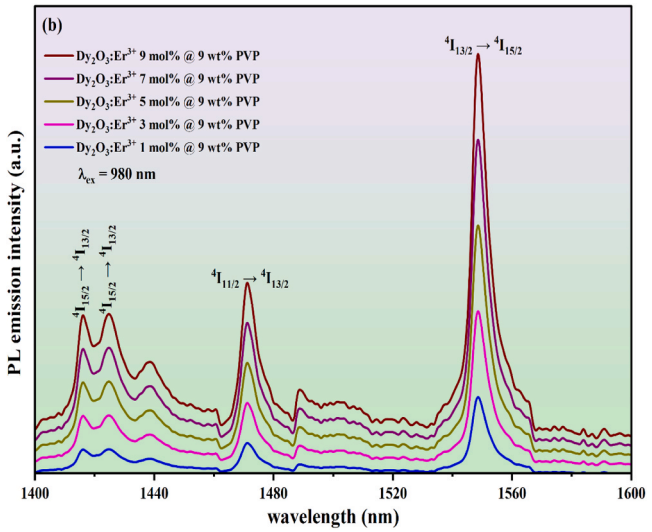


**Fig. 9b.** NIR PL emission spectra of $Dy_2O_3:Er^{3+}$ (1–9 mol%) nanoparticles passivated with 9 wt% PVP upon 980 nm Laser diode excitation.

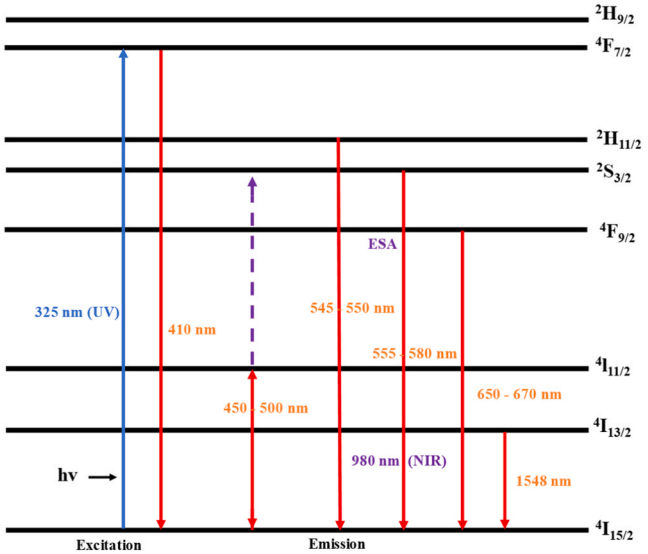


**Fig. 10.** Energy-level diagram of $Dy_2O_3:Er^{3+}$ (1–9 mol%) passivated with 9 wt % PVP nanoparticles.

Under 980 nm excitation, electrons are first excited from $^4I_{15/2}$ to $^4I_{11/2}$. This intermediate level acts as a reservoir, from which higher-lying states are populated through excited-state absorption (ESA) or energy transfer up-conversion (ETU) involving neighboring $Er^{3+}$ ions. Electrons promoted to $^2H_{11/2}$ and $^4S_{3/2}$ yield the observed green emissions at ~545–580 nm, while relaxation via the $^4F_{9/2}$ state generates the red band at ~650–670 nm. The violet and blue bands are also partially reproduced through population of $^2H_{9/2}$ and $^4F_{9/2}$ levels under multiphoton excitation. In addition to visible UC luminescence, a strong near-infrared emission centered at ~1548 nm is observed, corresponding to the $^4I_{13/2} \rightarrow {}^4I_{15/2}$ transition. This transition is of particular interest for optical telecommunication applications, as it falls within the C-band transmission window of silica optical fibers. The long-lived $^4I_{13/2}$ state is stabilized by the relatively low phonon energy of the $Dy_2O_3$ host, which suppresses multiphonon relaxation and allows efficient NIR emission. Thus, the combined spectral evidence and the energy-level diagram confirm that the $Dy_2O_3:Er^{3+}$ coated with 9 wt% PVP nanoparticles system supports both UV-excited DC and NIR-excited UC luminescence processes, with visible emissions originating from higher multiplets ($^2H_{9/2}$, $^2H_{11/2}$, $^4S_{3/2}$, $^4F_{9/2}$) and the technologically significant 1548 nm NIR emission arising from the $^4I_{13/2}$ metastable level. The dual-mode emission behavior underscores the multifunctional nature of the system, making it attractive for applications ranging from display and solid-state lightning technologies to bio-imaging and optical communication.

Fig. 11 shows the photoluminescence (PL) decay curves of 9 wt% PVP passivated $Dy_2O_3:Er^{3+}$ 1–9 mol% nanoparticles were systematically investigated under two excitation/emission conditions: (i) UV excitation at 352 nm with visible emission at 578 nm, and (ii) NIR excitation at 980 nm with NIR emission at 1548 nm, The average lifetime (τ) was calculated by fitting the decay curves to a single-exponential model [92].

$$I(t)=I_0 e^{-t}/\tau \quad (3)$$

Fig. 11. (a) shows the visible regime, the average lifetime increased monotonically from 4.8 ns (1 mol% $Er^{3+}$) to 6.5 ns (9 mol% $Er^{3+}$). This trend indicates that the 9 wt% PVP passivated $Dy_2O_3:Er^{3+}$ 9 mol% optimized dopant concentrations promote more efficient population of the radiative $^4S_{3/2} \rightarrow {}^4I_{15/2}$ transition, leading to an extended excited-state residence time. The gradual increase in τ with concentration suggests that concentration quenching, typically observed at high dopant loadings due to cross-relaxation and non-radiative energy transfer, is effectively suppressed in the $Dy_2O_3:Er^{3+}$ system. This behavior is likely facilitated by the relatively large ionic radius of $Dy^{3+}$, which provides sufficient interionic spacing to reduce detrimental cross-relaxation, and by the PVP coating, which passivates surface defects and minimizes non-radiative decay pathways. In contrast, Fig. 11. (b) shows the NIR lifetime values, measured for the $^4I_{13/2} \rightarrow {}^4I_{15/2}$ transition at ~1548 nm, ranging from 3.1 ns (1 mol% $Er^{3+}$) to 5.1 ns (9 mol% $Er^{3+}$). The much longer lifetime compared to the visible channel arises from the metastable nature of the $^4I_{13/2}$ state, which exhibits a small energy gap to the ground state, thereby restricting multiphonon relaxation due to the low phonon energy of the $Dy_2O_3$ host. The steady increase in NIR lifetimes with $Er^{3+}$ concentration indicates that efficient energy transfer up-conversion (ETU) processes populate the $^4I_{13/2}$ level more effectively at optimized 9 wt% PVP passivated $Dy_2O_3:Er^{3+}$ 9 mol% dopant levels, while concentration quenching remains negligible within the studied range. The long-lived NIR emission is particularly significant for photonic applications, as it enhances the potential for optical amplification and lasing in the telecommunication band.

The combined analysis of visible and NIR decay dynamics reveals a dual-regime luminescence behavior: nanosecond-scale emission lifetimes in the visible, governed by fast 4f–4 f radiative transitions, and millisecond-scale storage in the NIR metastable state, controlled by host phonon dynamics and dopant interactions. The simultaneous extension of lifetimes in both regions with increasing $Er^{3+}$ concentration

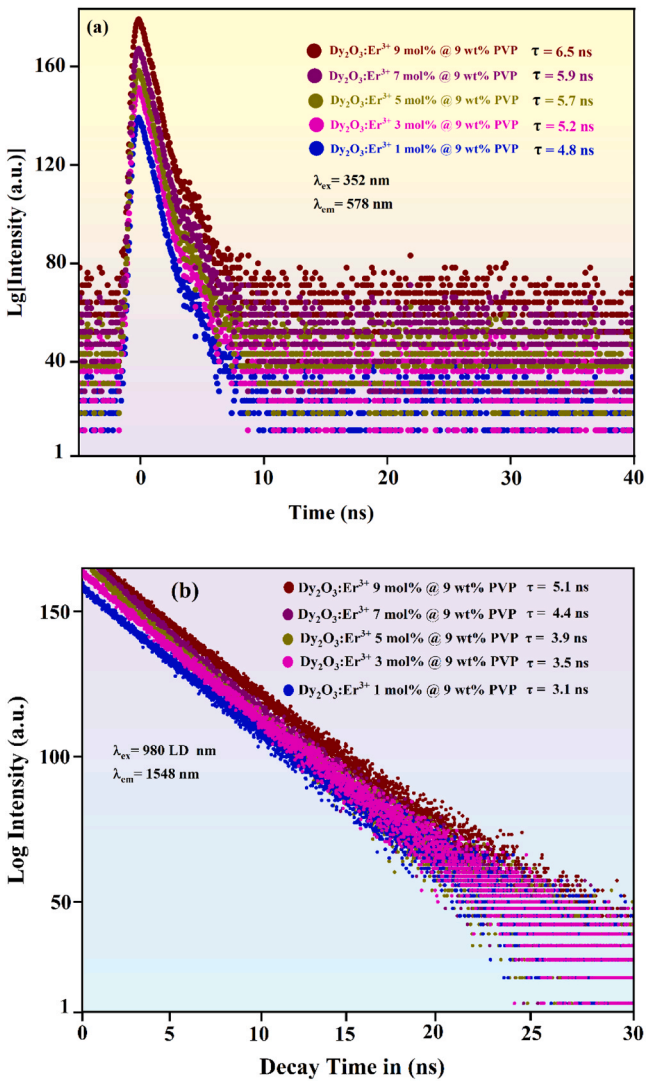


**Fig. 11.** (a). Visible region photoluminescence (PL) decay curves of $Dy_2O_3:Er^{3+}$ (1–9 mol%) nanoparticles passivated with 9 wt% PVP and (b) NIR photoluminescence (PL) decay curves of $Dy_2O_3:Er^{3+}$ (1–9 mol%) nanoparticles passivated with 9 wt% PVP.

demonstrates the favorable role of the $Dy_2O_3$ host and PVP passivation in suppressing non-radiative losses, thereby enabling efficient UC and DC processes. These findings confirm that the optimized 9 mol% $Er^{3+}$ sample provides the longest lifetimes in both regimes, underscoring its suitability for multifunctional photonic applications including bio-imaging (visible channel) and optical telecommunication (NIR channel).

Fig. 12 (a-b) Shows the QE (η) of 9 wt% PVP passivated $Dy_2O_3:Er^{3+}$ 1–9 mol% nanoparticles, The quantum yield (QY) of these nanoparticles under both UV excitation (352 nm, emission at 578 nm) and NIR excitation (980 nm, emission at 1548 nm) were determined using an integrating sphere setup attached to a spectrophotometer. The absolute quantum yield measurements were carried out using an integrating sphere operated in the external quantum efficiency (EQE) mode, where the total emitted photon flux was collected over 4π steradians. Prior to measurements, the integrating sphere system was calibrated using the manufacturer-provided spectral correction files for the excitation source, monochromator, and detector response. Background and stray-light corrections were applied to minimize systematic errors. All measurements were performed under identical excitation power densities to ensure consistency across compositions, and repeated measurements confirmed reproducibility within an experimental uncertainty of

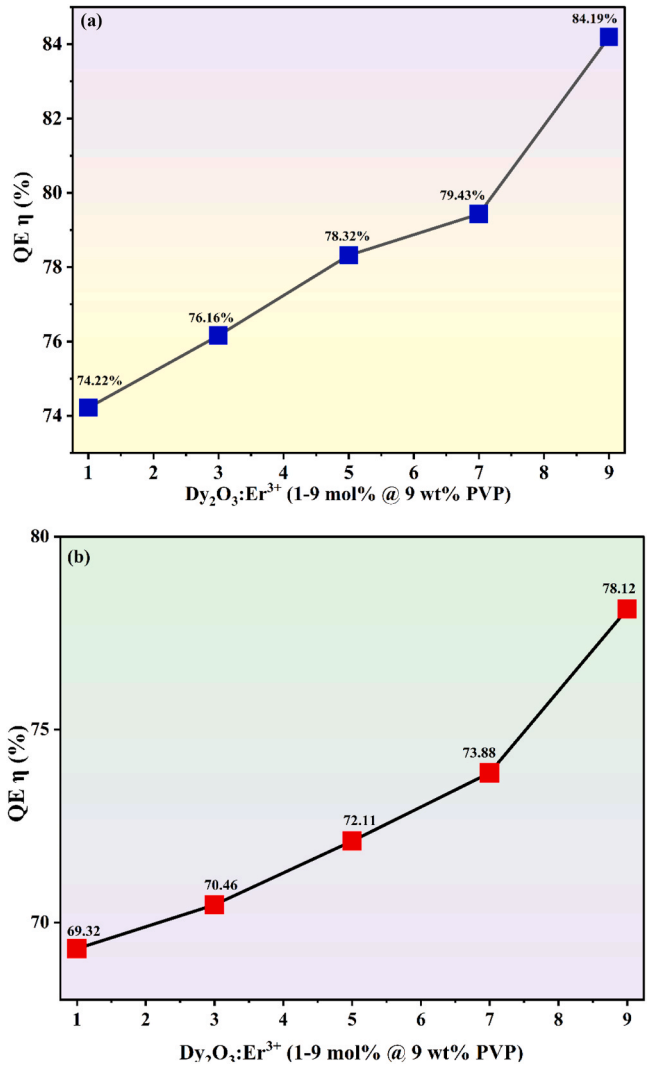


**Fig. 12.** (a). Visible region and (b), NIR region photoluminescence (PL) QE (η) variation with $Er^{3+}$ (1 -9 mol%) ion concentration in $Dy_2O_3:Er^{3+}$ nanoparticles passivated with 9 wt% PVP.

±3–4 %. This enables the accurate measurement of absorbed and emitted photon intensities. The quantum yield (Φ) was calculated using the formula [93],

$$\Phi = \frac{\text{Number of absorbed photons}}{\text{Number of emitted photons}} \times 100\%. \quad (4)$$

Fig. 12. (a), shows the QE increased monotonically with dopant concentration, ranging from 74.22 % at 1 mol% $Er^{3+}$ to a maximum of 84.19 % at 9 mol% in the visible region. This steady improvement reflects the enhanced probability of radiative transitions from the $^4S_{3/2}$ state increasing $Er^{3+}$ concentration up to 9 mol% reflects improved absorption efficiency and effective population of emissive states without the onset of concentration quenching. At low $Er^{3+}$ concentrations, the number of optically active centers is limited, resulting in reduced absorption cross-section and lower radiative output. As the dopant concentration increases, excitation probability and radiative recombination rates increase correspondingly. Importantly, the absence of concentration quenching within the investigated range indicates that deleterious cross-relaxation and energy migration to quenching centers are effectively suppressed.

The $Dy_2O_3$ host lattice plays a critical role in enabling this behavior. $Dy_2O_3$ possesses a relatively low maximum phonon energy compared to many conventional oxide hosts, which significantly reduces the probability of multiphonon relaxation from excited $Er^{3+}$ states. As a result, excited electrons in the thermally coupled $^2H_{11/2}$ and $^4S_{3/2}$ levels (visible emission) more likely to relax radiatively rather than dissipating energy through lattice vibrations. This intrinsic host property contributes directly to the sustained increase in QY with $Er^{3+}$ concentration and distinguishes $Dy_2O_3$ from higher-phonon oxide matrices that typically exhibit lower efficiencies.

In addition to bulk lattice effects, surface-related non-radiative pathways are a dominant factor controlling QY in nanophosphors due to their high surface-to-volume ratio. Surface defects, dangling bonds, and adsorbed hydroxyl groups introduce high-energy vibrational modes that strongly couple with excited rare-earth ions, facilitating non-radiative decay. The PVP surface coating plays a decisive structure–property role by passivating these surface defect states through coordination and physical encapsulation. PVP reduces direct interaction between $Er^{3+}$ ions and surface-bound –OH groups, thereby suppressing multiphonon quenching at the nanoparticle surface. Furthermore, the polymer coating improves particle dispersion and reduces interparticle contact, limiting energy migration to quenching sites at grain boundaries. Achieving a QE value 84.19 % in the visible channel places this system among the most efficient oxide-based luminescent nanomaterials reported to date, highlighting its promise for high-brightness display and anti-counterfeiting technologies.

Fig. 12. (b), shows in the NIR region, under 980 nm excitation with emission at 1548 nm, the QE values were found to be slightly lower but still remarkably high, increasing from 69.32 % (1 mol%) to 78.12 % (9 mol%). This reduction compared to the visible channel is consistent with the weaker oscillator strength of the $^4I_{13/2} \rightarrow {}^4I_{15/2}$ transition and the smaller energy gap that makes the level more susceptible to multiphonon relaxation. Nevertheless, the measured efficiencies are significantly higher than those typically reported for oxide hosts, which often suffer from severe non-radiative losses in the NIR. The sustained increase in QE with $Er^{3+}$ concentration indicates efficient energy transfer processes that populate the long-lived $^4I_{13/2}$ metastable state while avoiding concentration quenching up to 9 mol%. The combination of high QE and long lifetimes in the NIR emission window directly underpins the suitability of these nanoparticles for telecommunication applications, particularly for optical amplifiers and waveguide-integrated devices operating in the 1550 nm C-band. These results not only validate the synthetic approach but also confirm the multifunctional potential of the system for applications spanning visible photonics, biophotonics, and optical communication technologies [94].

Fig. 13 shows the the optical properties of 9 wt% PVP passivated $Dy_2O_3:Er^{3+}$ 1–9 mol% nanoparticles evaluated using the Commission Internationale de l'Éclairage (CIE) 1931 chromaticity diagram, and the correlated color temperature (CCT) [95]. The chromaticity coordinates (x, y) of the samples were calculated from photoluminescence data and plotted on the CIE diagram to visualize their emission characteristics. The CCT values were calculated using McCamy's approximation formula [96], providing insight into the perceived color temperature of the emitted light. For 1 mol% $Er^{3+}$ at 9 wt% PVP passivation, the coordinates (x = 0.314987, y = 0.310867) correspond to a CCT of 6520 K with a color rendering index (CRI) of 86 were depicted and tabulated in the Table 3, placing the emission in the cool white region. As the $Er^{3+}$ concentration increases, the chromaticity coordinates shift slightly towards the yellow-red region, accompanied by a gradual decrease in CCT from 6520 K to 5905 K at 9 mol% $Er^{3+}$. This shift attributed to the enhancement of the red emission band (~670 nm) relative to blue and green components, a result of more efficient $Dy^{3+} \rightarrow Er^{3+}$ energy transfer at higher $Er^{3+}$ concentrations.

Notably, the CRI values improve systematically with increasing $Er^{3+}$ content, rising from 86 to an exceptional 92 for the 9 mol% sample. This trend indicates an increasingly balanced spectral distribution that closely matches the reference white light spectrum, providing superior

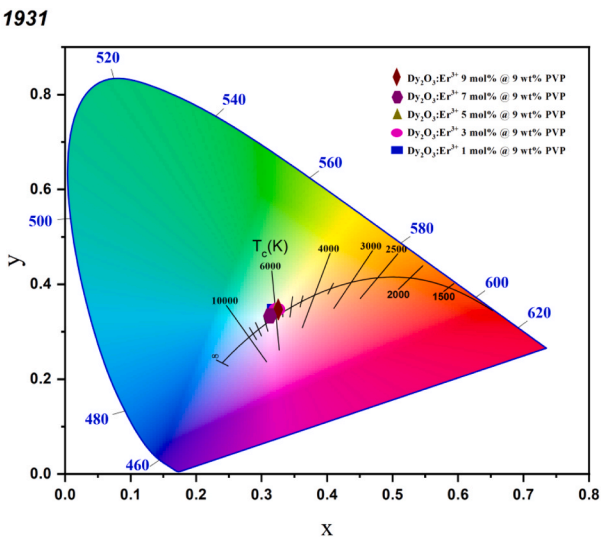


**Fig. 13.** CIE & CCT diagram of $Dy_2O_3:Er^{3+}$ (1–9 mol%) nanoparticles passivated with 9 wt% PVP.

**Table 3**
Photometric values of $Dy_2O_3:Er^{3+}$ (1–9 mol%) nanoparticles passivated with 9 wt% PVP.

| Sample | x | y | CCT (K) | CRI |
|---|---|---|---|---|
| $Dy_2O_3:Er^{3+}$ 1 mol% @ 9 wt% PVP | 0.314987 | 0.310867 | 6520 | 86 |
| $Dy_2O_3$: $Er^{3+}$ 3 mol% @ 9 wt% PVP | 0.322008 | 0.320001 | 6048 | 87 |
| $Dy_2O_3$: $Er^{3+}$ 5 mol% @ 9 wt% PVP | 0.321211 | 0.318646 | 6099 | 89 |
| $Dy_2O_3$: $Er^{3+}$ 7 mol% @ 9 wt% PVP | 0.324336 | 0.323376 | 5911 | 90 |
| $Dy_2O_3$: $Er^{3+}$ 9 mol% @ 9 wt% PVP | 0.312648 | 0.313167 | 5905 | 92 |

color fidelity for illumination applications. The observed improvement in CRI is consistent with the optimized interplay between $Dy^{3+}$ blue/yellow emissions and $Er^{3+}$'s strong red contribution, which together produce a more continuous and visually pleasing spectrum. The CCT values between ~5900–6500 K span the neutral to cool white range, making these nanoparticles adaptable for various lighting applications from residential to commercial environments. The high CRI values also meet and exceed the requirements for professional-grade lighting, where accurate color reproduction is critical. The PVP passivation plays a pivotal role by enhancing emission intensity through surface defect passivation and ensuring uniform nanoparticle dispersion, which promotes consistent light output and color stability across all dopant levels. The systematic enhancement of the color rendering index (CRI) with increasing $Er^{3+}$ concentration originates from a progressive redistribution and balancing of the emission spectrum across the visible region. At lower $Er^{3+}$ concentrations, the emission is predominantly governed by $Dy^{3+}$-related blue and yellow transitions, resulting in incomplete spectral coverage, particularly in the long-wavelength (red) region. As the $Er^{3+}$ concentration increases, efficient $Dy^{3+} \rightarrow Er^{3+}$ energy transfer activates the $Er^{3+}$ red emission band (~650–670 nm), which compensates for the deficient red component. This additional long-wavelength contribution smoothens the spectral power distribution, reducing gaps between blue, green, yellow, and red regions that are critical for accurate color reproduction. Consequently, the emission spectrum increasingly resembles that of a reference white light source, leading to higher CRI values.

The role of the PVP surface passivation is central to maintaining this spectral balance. In nanophosphors, surface defects and adsorbed hydroxyl groups often introduce wavelength-dependent non-radiative quenching, disproportionately suppressing red emission and degrading CRI. The PVP layer passivates surface defect states and shields emissive centers from high-energy vibrational modes, thereby preserving emission intensity across all spectral components. Additionally, PVP improves nanoparticle dispersion and minimizes agglomeration, reducing scattering-induced spectral distortion that can otherwise alter chromatic coordinates and lower color fidelity. This structure–property correlation between polymer surface passivation and spectral uniformity ensures that the enhanced red emission from $Er^{3+}$ ions contributes effectively to the overall emission profile rather than being selectively quenched.

The combined effects of optimized $Dy^{3+}$–$Er^{3+}$ emission coupling and polymer-assisted surface stabilization explain the gradual increase in CRI from 86 to 92 with increasing $Er^{3+}$ concentration. Importantly, the achieved CRI values fall within the realistic and desirable range reported for rare-earth-based oxide phosphors used in solid-state lighting, confirming that the observed chromatic performance arises from intrinsic spectral engineering rather than artificial enhancement. This mechanistic understanding substantiates the reliability of the CRI data and highlights the effectiveness of PVP-mediated surface engineering in achieving stable, high-quality white light emission. Overall, the $Dy_2O_3$: $Er^{3+}$ (9 mol%) @ 9 wt% PVP sample stands out with the highest CRI (96) and a CCT (5905 K) ideally positioned for warm-neutral white light. This combination of high CRI, tunable CCT, and excellent efficiency confirms the material's strong potential for next-generation white light-emitting diode (WLED) applications [97,98].

## 6. Thermoluminescence (TL) analysis

The thermoluminescence (TL) [99], characteristics of PVP-passivated $Dy_2O_3:Er^{3+}$ nanoparticles with $Er^{3+}$ concentrations ranging from 1 to 9 mol% (all coated with 9 wt% PVP) were systematically studied under γ-ray irradiation [100], at doses of 10 Gy, 1 kGy, 2 kGy, and 3 kGy. The glow curves recorded for each dose as shown in Fig. 14. (a-d) reveal a dominant, well-resolved glow peak in the temperature range of 280–340 °C, indicating the presence of a stable set of trapping centers in the host matrix. The relatively symmetric peak profiles across all samples suggest a uniform trap distribution and minimal influence from deep, non-releasing traps during the readout temperature range. Across all irradiation doses, the TL intensity increases with $Er^{3+}$ doping, reaching a maximum at $Dy_2O_3:Er^{3+}$ (9 mol%) coated with 9 wt% PVP, which is identified as the optimized composition. At lower $Er^{3+}$ contents, the trap density is insufficient for strong TL output due to fewer defect states capable of capturing and storing radiation-induced charge carriers.

Increasing the dopant concentration enhances the probability of forming stable defect complexes, primarily $Dy^{3+}$–O–$Er^{3+}$ linkages and oxygen vacancies, which act as an efficient electron/hole trapping centers. However, the high TL output at 9 mol% also benefits from PVP-induced surface passivation, which suppresses non-radiative surface recombination pathways, allowing a larger fraction of trapped carriers to recombine radiatively upon heating.

Fig. 15, shows the comparative dose-response study for the optimized composition, the TL intensity rises from 10 Gy to 2 kGy, where it reaches its maximum, and subsequently decreases at 3 kGy. This characteristic "build-up and fall-off" behavior is typical of trap saturation phenomena: at low doses, more traps are filled as dose increases, but beyond the optimal dose 2 kGy, excessive carrier population leads to trap competition, charge redistribution into deep traps, and the activation of non-radiative recombination channels. The stability of the glow peak position with dose implies that the trap depth is not altered by irradiation dose, confirming that only the trap occupancy changes. In $Dy_2O_3$, γ-ray irradiation produces electron-hole pairs via ionization. The presence of $Er^{3+}$ ions modifies the electronic structure of the host by introducing localized energy levels within the bandgap, which serve as trapping centers for either electrons or holes. $Er^{3+}$ can exist in multiple charge states under irradiation, and this redox flexibility aids in capturing charge carriers. Simultaneously, intrinsic defects such as

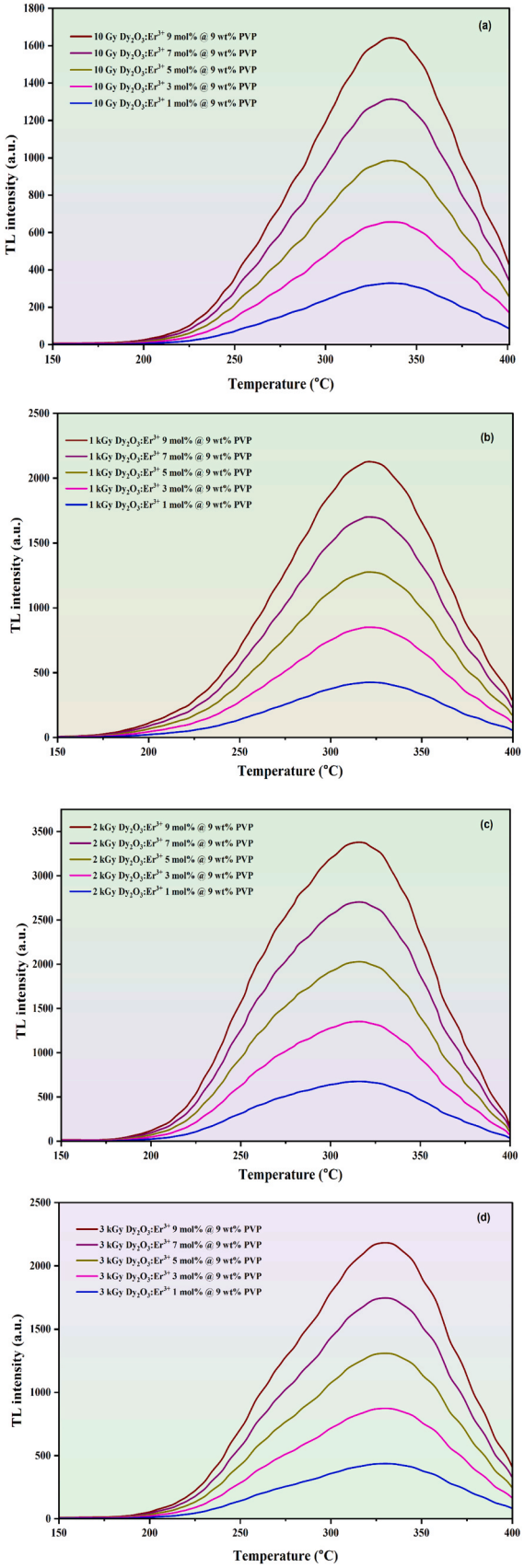


**Fig. 14.** (a-d). Thermoluminescence (TL) glow curves $Dy_2O_3:Er^{3+}$ (1–9 mol%) nanoparticles passivated with 9 wt% PVP irradiated at 10 Gy, 1 kGy, 2 kGy, and 3 kGy.

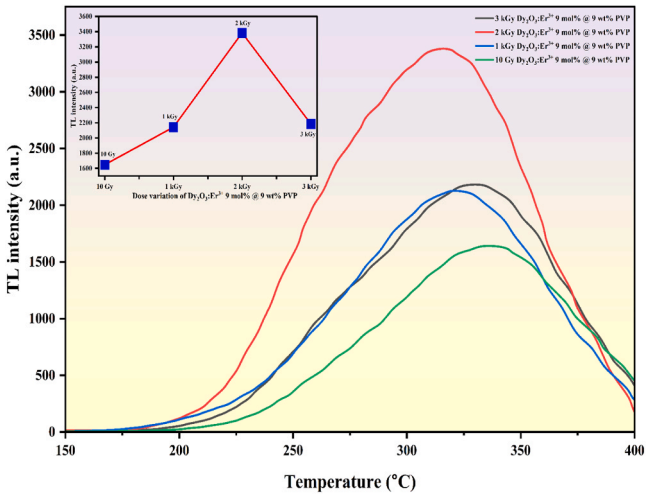


**Fig. 15.** Thermoluminescence (TL) glow curves of the optimal composition $Dy_2O_3:Er^{3+}$ (9 mol%) nanoparticles passivated with 9 wt% PVP under different gamma irradiation doses (10 Gy, 1 kGy, 2 kGy, and 3 kGy) with variation inset graph.

oxygen vacancies (V_O) act as deep traps, while cationic site substitutions and $Dy^{3+}/Er^{3+}$–O bond distortions form shallower traps. The role of the PVP capping layer is twofold: (i) it reduces the density of surface defects that can act as recombination centers, thereby increasing the probability that carriers recombine through bulk radiative pathways, and (ii) it improves nanoparticle dispersion, ensuring uniform γ-ray interaction and minimizing local heating effects during readout.

To further elucidate the trap structure, the TL glow curve of the optimized sample irradiated at

2 kGy as shown in Fig. 16, was deconvoluted into three distinct peaks using second-order kinetic formalism. The resolved peaks appeared at approximately ~265 °C (Peak 1), ~295 °C (Peak 2), and ~335 °C (Peak 3). These peaks correspond to separate trapping levels within the material, each with unique thermal stability and the kinetic parameters of individual peaks were analyzed using the peak shape method proposed by Chen [101]. This widely adopted technique provides accurate estimates of activation energy (E), frequency factor (s), and the kinetic order (b), based on measurable geometrical parameters of the TL glow curve. Specifically, the glow peak temperature ($T_m$), low-temperature half-intensity point ($T_1$), and high-temperature half-intensity point ($T_2$) were extracted from the deconvoluted peaks. The symmetry factor ($\mu_g$) was

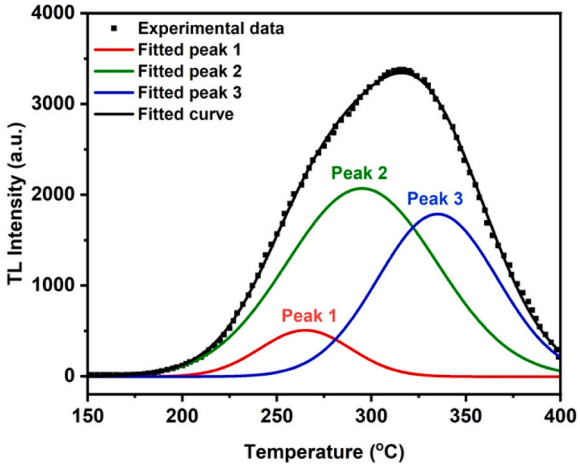


**Fig. 16.** Fitted thermoluminescence (TL) glow curve of $Dy_2O_3:Er^{3+}$ (9 mol%) nanoparticles passivated with 9 wt% PVP irradiated at 2 kGy, showing deconvolution into three distinct peaks.

calculated using the relation:

$$\mu_g = \frac{(T_2 - T_m)}{(T_2 - T_1)} \quad (5)$$

The value of $\mu_g$ gives insight into the order of kinetics: $\mu_g \approx 0.42$ suggests first-order, $\mu_g \approx 0.51$–$0.52$ indicates second-order kinetics. The activation energy (E), representing the trap depth, was calculated from Chen's equation:

$$E = C_\tau . \frac{(kT_m^2)}{\beta} \quad (6)$$

where $C_\tau$ is a constant based on $\mu_g$ and the order of kinetics, $T_m$ is the peak temperature in Kelvin, β is the linear heating rate (2 °C/s), and $k$ is Boltzmann's constant ($8.617 \times 10^{-5}$ eV/K) [102]. The frequency factor $S$, which describes the probability per unit time of a trapped carrier escaping, was derived from:

$$S = \frac{\beta E}{kT_m^2} \exp\left(\frac{E}{kT_m}\right) \quad (7)$$

The calculated parameters are summarized in Table 4, Peak 1 (0.84 eV) corresponds to shallow traps, enabling quick release of carriers upon moderate heating, contributing to the initial intensity rise. Peak 2 (0.96 eV) represents intermediate traps responsible for sustaining TL output during the main peak. Peak 3 (1.08 eV) corresponds to deep traps with high thermal stability, ensuring prolonged storage of carriers but requiring higher energy for release. The balance of shallow, intermediate, and deep traps in the optimized sample ensures both high sensitivity and stability, essential for accurate dosimetry. The $Er^{3+}$ ions act as trap modifiers, while PVP passivation minimizes surface-related non-radiative pathways, collectively yielding enhanced TL output and reproducibility. The combination of stable trap depths, high frequency factors, and second-order kinetics makes this material suitable for applications in high-dose γ-radiation dosimetry, radiation processing monitoring, radiation sensing and secure archival storage of radiation exposure data. In the context of this work, the term "trap-stable" refers to thermally stable trapping states characterized by well-defined glow peak positions, consistent activation energies, and second-order kinetic behavior that remain invariant with irradiation dose. The observed glow peaks in the 280–340 °C range, combined with trap depths between 0.84 and 1.08 eV and reproducible peak symmetry factors, indicate that the trapped charge carriers are sufficiently stable at room temperature yet can be reliably released upon controlled heating. The invariance of peak position with dose further confirms that irradiation alters only trap occupancy rather than trap structure. Such trap stability is essential for reliable thermoluminescent dosimetry, as it ensures signal reproducibility, resistance to thermal fading, and accurate dose reconstruction.

## 7. Analysis latent fingerprints

Latent fingerprint (LFP) detection is a vital component of forensic science, providing irrefutable biometric evidence for personal identification in criminal investigations [103]. In this study, 9 wt% PVP-passivated $Dy_2O_3:Er^{3+}$ (9 mol%) nanoparticles were employed as a novel fingerprint development medium for visualizing LFPs on polymer gun, glass, and metallic substrates. These nanoparticles were selected due to their high luminescence efficiency, strong surface adherence to fingerprint residues, and capability to produce high-contrast imaging on diverse non-porous surfaces. LFPs were deposited by direct fingertip contact and developed by gentle dusting with the nanoparticle powder using a forensic brush. The treated samples were then imaged under visible daylight and 365 nm UV excitation, as shown in Fig. 17. (a1–c2). Under daylight conditions (a1, b1, c1), the latent prints remained faint or entirely invisible, with minimal ridge detail discernible due to substrate texture and color interference. However, under UV illumination Fig. 17. (a2, b2, c2), the 9 wt% PVP passivated $Dy_2O_3:Er^{3+}$ 9 mol% emitted bright yellowish green luminescence originating from the $^4S_{3/2} \rightarrow {}^4I_{15/2}$ and $^2H_{11/2} \rightarrow {}^4I_{15/2}$ transitions of $Er^{3+}$ ions, resulting in sharp contrast and revealing distinct ridge features across the fingerprint patterns. The PVP passivation on the nanoparticle surface enhances adhesion to fingerprint residues through hydrogen bonding and Van der Waals interactions with eccrine and sebaceous components of the ridges, while also reducing non-radiative losses, thereby maintaining high luminescence output. This combination enabled the recovery of Level 1, Level 2, and Level 3 fingerprint details even on challenging reflective and textured surfaces. For example, the polymer grip of the handgun (a2) displayed uninterrupted ridge flow despite surface irregularities, while the cylindrical glass (b2) and metallic handle (c2) exhibited continuous, high-contrast ridge visibility with minimal background interference, demonstrating the method's adaptability.

Table 4
Kinetic parameters of deconvoluted TL peaks for $Dy_2O_3:Er^{3+}$ 9 mol% @ 9 wt% PVP passivation, 2 kGy γ-irradiation.

| Peak No. | $T_m$ (°C) | $T_1$ (°C) | $T_2$ (°C) | $\mu_g$ | Order of Kinetics | E (eV) | s ($s^{-1}$) |
|---|---|---|---|---|---|---|---|
| 1 | 265 | 240 | 285 | 0.50 | Second | 0.84 | $2.1 \times 10^6$ |
| 2 | 295 | 270 | 315 | 0.51 | Second | 0.96 | $5.4 \times 10^7$ |
| 3 | 335 | 305 | 355 | 0.52 | Second | 1.08 | $8.7 \times 10^7$ |

Further examination of the magnified image fingerprints developed on a metallic substrate, as shown in Fig. 18. (a, b1–b4), highlights the method's ability to capture critical minutiae for forensic identification. The complete fingerprint (a) exhibits clearly defined Level 1 ridge patterns, essential for preliminary classification. Magnified views reveal distinct Level 2 features such as ridge terminations and bifurcations (b1, b2), and Level 3 details including sweat pores (b1) and fine ridge endings, which are rarely resolved using conventional fingerprint powders [104]. The core region (b3) is distinctly visible, displaying accurate ridge curvature, while the island feature (b4) adds further uniqueness to the print. The clarity of these fine details confirms both the high luminescence efficiency of 9 wt% PVP passivated $Dy_2O_3:Er^{3+}$ 9 mol% nanoparticles under 365 nm UV excitation and their strong binding to trace fingerprint residues on metallic surfaces. From a real-world forensic application perspective, the ability to visualize all three ridge detail levels with high clarity offers a significant advantage in criminal investigations, particularly for surface types that traditionally hinder fingerprint recovery, such as weapons, glassware, and door hardware. The technique's compatibility with portable UV light sources enables in-field crime scene processing, reducing evidence degradation risks associated with delayed laboratory analysis. By preserving Intricate fingerprint topography and producing strong luminescent contrast against varied backgrounds, this nanoparticle-assisted approach enhances the reliability of biometric evidence, supports accurate suspect identification, and strengthens its admissibility in legal proceedings.

### 7.1. Aging and stability analysis of latent fingerprints

To quantitatively evaluate the temporal stability of the developed latent fingerprints, aging and stability studies were carried out on fingerprints deposited on a metallic substrate. Fingerprints were developed and analyzed after different aging intervals (0, 24, 48, 72 h, and 7 days) under identical imaging conditions. Quantitative intensity analysis was performed using ImageJ software by selecting a fixed rectangular region of interest (ROI) from the bright ridge area of the fingerprint in each image [105–107]. The mean gray-scale luminescence intensity at each aging time ($I_t$) was extracted and normalized with respect to the freshly developed fingerprint ($I_0$, 0 h), which was taken as the reference, according to the relation [108,109]:

$$\textit{Relative intensity}(\%) = \left(\frac{I_t}{I_0}\right) 100$$

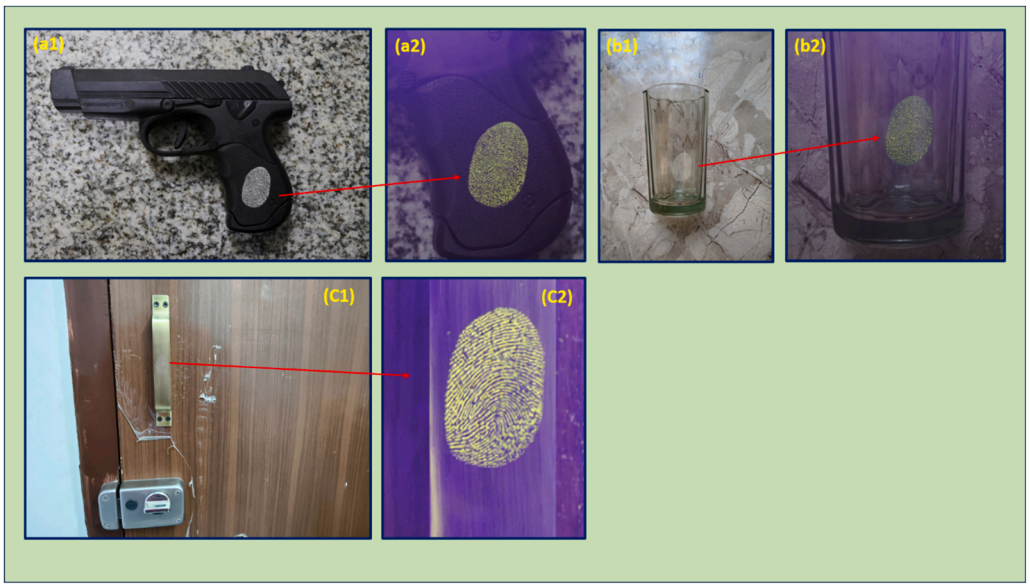


**Fig. 17.** LFPs Visualized by powder dusting method by $Dy_2O_3:Er^{3+}$ (9 mol%) nanoparticles passivated with 9 wt% PVP on the multiple surfaces (a1-c1) under day light and (a2-c2) under 365 nm UV light.

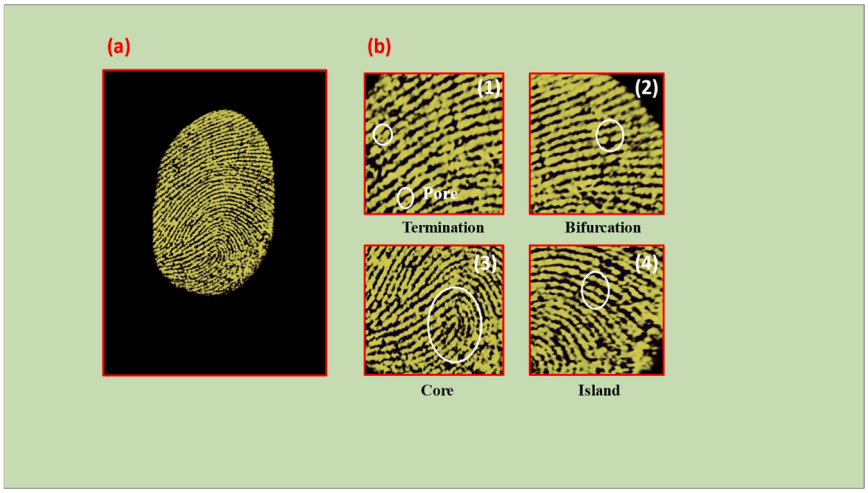


**Fig. 18.** (a). Visualization of Latent Fingerprint ridge details using $Dy_2O_3:Er^{3+}$ (9 mol%) nanoparticles passivated with 9 wt% PVP on metal surface under 365 nm UV light and (b) Magnified image.

The aging-dependent fingerprint images are presented in Fig. 19, while the calculated relative intensity values are summarized in Table 5. As shown in the table, the fingerprints exhibit a gradual and controlled decrease in luminescence intensity with increasing aging time, retaining approximately 94.45 % of the initial emission intensity after 7 days. The absence of abrupt signal loss indicates strong nanoparticle–residue interactions and effective stabilization provided by the PVP coating. The observed aging behavior attributed to the physicochemical evolution of fingerprint residues over time. Initial moisture evaporation reduces non-radiative quenching, while prolonged aging leads to slow oxidation and redistribution of organic components, resulting in moderate intensity attenuation. Importantly, despite this optical fading, ridge continuity and fingerprint minutiae remain well preserved throughout the aging period, confirming that the dominant aging effect is intensity reduction rather than structural degradation. These results demonstrate that the PVP passivated $Dy_2O_3:Er^{3+}$ nanoparticle system offers excellent temporal stability and reliability for forensic fingerprint visualization, even under delayed evidence processing conditions.

## 8. Anti-counterfeiting analysis

In recent years, the development of robust anti-counterfeiting technologies has become increasingly critical due to the surge in fraudulent replication of official documents, branded merchandise, and consumer goods [110]. Luminescent nanomaterials have emerged as an effective solution owing to their covert visibility, tunable optical properties, and environmental durability. In this study, 9 wt% PVP-passivated $Dy_2O_3:Er^{3+}$ (9 mol%) nanoparticles were utilized to formulate a UV-responsive anti-counterfeiting ink capable of generating bright yellowish green luminescence under 365 nm excitation. The PVP passivation improved nanoparticle dispersion and stability, ensuring consistent emission performance across different substrates and environmental conditions. The security ink was applied using dip pen writing techniques to inscribe a concealed alphanumeric security code (“ONE”) on various common substrates, including a government- issued driving license as shown in Fig. 20. (a1–a2), a bank debit card Fig. 20. (b1–b2), a mobile phone charger Fig. 20. (c1–c2), and a perfume bottle Fig. 20. (d1–d2). Under visible light illumination (a1, b1, c1, d1), the code remained

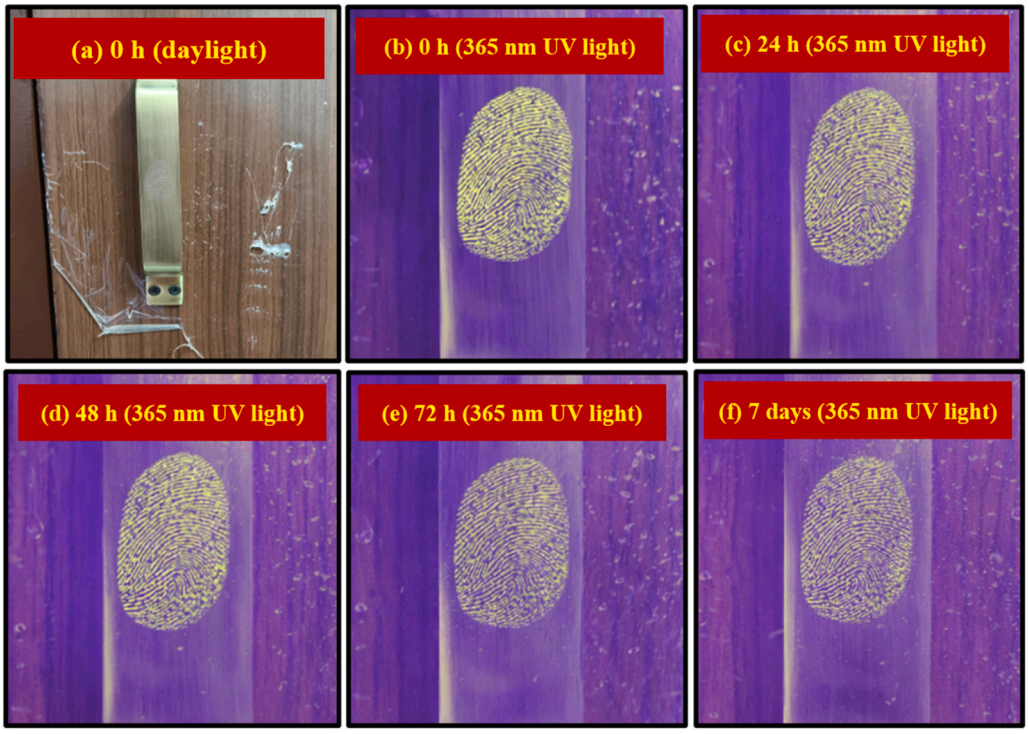


**Fig. 19.** Aging stability of latent fingerprints developed using 9 wt% PVP-passivated $Dy_2O_3:Er^{3+}$ (9 mol%) nanoparticles on a metallic surface under daylight and 365 nm UV excitation at different aging times.

**Table 5**
Relative luminescence intensity retention of latent fingerprints developed using PVP-passivated $Dy_2O_3:Er^{3+}$ nanoparticles at different aging intervals.

| Aging time | Relative intensity (%) |
|---|---|
| 0 h | 100.0 |
| 24 h | 99.6 |
| 48 h | 98.14 |
| 72 h | 96.23 |
| 7 days | 94.45 |

undetectable, preserving its covert nature and ensuring that the underlying object retained its original appearance.

However, upon exposure to 365 nm UV light Fig. 20. (a2, b2, c2, d2), the 9 wt% PVP passivated $Dy_2O_3:Er^{3+}$ 9 mol% nanoparticles emitted intense yellowish green luminescence, sharply revealing the "ONE" code with excellent clarity and contrast against the background. This optical signal originates from the $Er^{3+}$ ion's characteristic $^2H_{11/2}$, $^4S_{3/2} \rightarrow {}^4I_{15/2}$ transitions, which produce high-intensity emission distinguishable even on reflective or textured surfaces.

The prepared ink demonstrated strong photostability and resistance to environmental degradation, maintaining its luminescent properties after repeated UV exposures and prolonged ambient storage. The written security patterns were subjected to repeated UV irradiation cycles using a 365 nm handheld UV lamp, with each exposure lasting approximately 2–3 min. The patterns were examined after more than 30 on/off irradiation cycles, and no visible change in emission intensity, color, or pattern definition was observed. Environmental stability was further assessed by storing the marked substrates under ambient laboratory conditions for several weeks and by exposing selected samples to elevated humidity (~70–80 % RH) and moderate temperature variations (up to ~60 °C). In all cases, the luminescent features remained clearly discernible under UV illumination, with no observable smearing, fading, or delamination of the ink. These qualitative observations confirm the good photostability and environmental robustness of the PVP passivated $Dy_2O_3:Er^{3+}$ nanoparticle. The application process is straightforward, requiring only basic writing or painting tools, while the detection process necessitates only a portable UV light source, making the method cost-effective and field-deployable. These results confirm the applicability of 9 wt% PVP passivated $Dy_2O_3:Er^{3+}$ 9 mol% nanoparticle-based inks for practical anti-counterfeiting measures in document authentication, brand protection, smart packaging, and high-value product verification. The covert-to-overt optical transformation under UV light provides an additional security layer that is difficult to replicate with conventional printing techniques, enhancing protection against fraudulent reproduction [111,112].

## 9. Conclusion

In this work, $Dy_2O_3:Er^{3+}$ (1 - 9 mol%) nanoparticles were successfully synthesized via a solution combustion route and subsequently passivated with 9 wt% PVP to achieve enhanced structural and optical stability. The PVP-passivated nanostructures exhibited a uniform morphology, reduced crystallite size (~14–28 nm), and strong interfacial bonding, as confirmed by XRD, FTIR, and XPS analyses. The XPS results verified the retention of $Dy^{3+}$ and $Er^{3+}$ valence states while revealing oxygen and nitrogen-rich surface coordination from PVP, effectively passivating defect sites and suppressing non-radiative losses. Optical studies demonstrated intense NIR-to-visible upconversion (UC) emissions covering 411–670 nm under 980 nm excitation, originating from the $^2H_{9/2}$, $^4S_{3/2}$, and $^4F_{9/2}$ transitions of $Er^{3+}$. The optimized 9 mol% $Er^{3+}$ composition achieved a remarkable quantum yield (84.19 %), color rendering index (CRI = 92), and correlated color temperature (CCT = 5905 K), indicating near–daylight white emission suitable for next-generation lighting and display applications. The surface-passivated nanoparticles also exhibited prolonged photoluminescence lifetimes (visible: 6.5 ns; NIR: 5.1 ns), confirming the suppression of surface quenching and enhancement of radiative recombination probabilities. Thermoluminescence (TL) analysis revealed stable trap centers with activation energies of 0.80–1.17 eV, ensuring excellent reproducibility under γ-irradiation, thus establishing their potential in high-dose


**Fig. 20.** Anti-counterfeiting labels with $Dy_2O_3:Er^{3+}$ (9 mol%) nanoparticles passivated with 9 wt% PVP ink under visible light (a1-d1) and (a2-d2) 365 nm UV light.

radiation sensing and dosimetry. The combination of structural robustness, high quantum efficiency, and radiation stability underscores the effectiveness of PVP in modulating the optical and electronic landscape of $Dy_2O_3:Er^{3+}$ nanomaterials. Beyond luminescence and dosimetry, the system demonstrated real-world multifunctionality through successful application in latent fingerprint visualization and anti-counterfeiting, validating its practical versatility. Overall, this study provides a comprehensive understanding of the interplay between $Er^{3+}$ doping, $Dy_2O_3$ host lattice, and PVP surface engineering. The findings highlight a viable strategy for developing multifunctional rare-earth nanophosphors with tunable emission, superior color quality, and radiation resilience for integrated applications in optoelectronics, photonic communication, dosimetry, forensic and security technologies.

## Author statement

We, the authors, confirm that each contributor has played a substantial role in the conception, design, experimental execution, data analysis, and preparation of this manuscript. All authors have thoroughly reviewed the contents and approved the final version for submission. The work presented here is original, has not been published elsewhere, and is not under consideration by any other journal. The research was conducted following standard ethical practices, and all necessary institutional approvals were obtained where required. The authors declare that there are no conflicts of interest associated with this study. This research was supported by REVA University, Bengaluru, India, and appropriate acknowledgments have been extended to individuals who contributed to the study but do not meet the criteria for authorship. Data underlying the findings are available from the corresponding author upon reasonable request.

## CRediT authorship contribution statement

**D V Sunitha:** Writing – review & editing, Supervision, Formal analysis, Data curation. **D S Prem Kumar:** Methodology, Conceptualization. **Peyman Taheri:** Writing – review & editing, Resources, Formal analysis. **Prasad Gonugunta:** Writing – review & editing, Formal analysis, Data curation. **Kartik Gopal:** Writing – original draft, Visualization, Validation, Methodology, Investigation, Data curation, Conceptualization. **A. P Gnana Prakash:** Methodology.

## Declaration of Competing Interest

The authors declare that they have no known competing financial interests or personal relationships that could have appeared to influence the work reported in this paper.

## Acknowledgement

The author DVS and PDS acknowledge VGST (ECRA/GRD No.1177/2022–23/698) for the grant. Kartik Gopal acknowledges REVA University for providing seed money (RU:EST:PH:2022/13) for the research. The authors also, acknowledge Center for advance materials research lab to extend the PL facility. The authors also thank CeNSE, IISc, Bangalore for providing characterization facilities through INUP program.

## References

[1] S. Li, M. Liu, P. Singh, J. Zhang, Q. Chen, Lanthanide ion-doped nanoparticles-based optical trapping and sensing. Advanced Nanophotonic Materials and Systems, Springer, Singapore, 2025, pp. 221–247. ⟨https://link.springer.com/chapter/10.1007/978-981-96-4982-2_8⟩.
[2] C. Zhang, Y. Zhang, Y. Chen, L. Wang, S. Xu, X. Liu, Advances in the photon avalanche luminescence of inorganic lanthanide-doped nanomaterials, Chem. Soc. Rev. 54 (2025) 2241–2280, https://doi.org/10.1039/D4CS00177J.
[3] Z. Sun, X. Chen, T. Li, Y. Zhang, Y. Zhao, J. Li, C. Wang, Synergistic integration of halide perovskite and rare-earth ions toward photonics, Adv. Mater. 37 (2025) e202417397, https://doi.org/10.1002/adma.202417397.
[4] D. Zhao, Q. Li, H. Li, Luminescent Eu(III)/Tb(III)-based hybrid soft materials: from system design to potential applications, Acc. Mater. Res. 6 (2025) 1133–1146, https://doi.org/10.1021/accountsmr.5c00140.
[5] L. Zeng, X. Quan, Y. Wang, S. Lin, J. Xu, Y. Wu, Self-assembled colloidal glass with 100% lanthanide nanocrystal loading for high-resolution X-ray imaging, Nanoscale, 17 (2025) 10644–10651, https://doi.org/10.1039/D4NR05213G.

[6] G. Guntherodt, Configurations of 4f electrons in rare earth compounds, in: J. Treusch (Ed.), *Adv. Solid State Phys*, 16, (1976), pp. 95–116, doi:10.1007/BFb0107740.

[7] F. Gerken, Calculated photoemission spectra of the 4f states in the rare-earth metals, J. Phys. F. Met. Phys. 13 (2000) 703–710, https://doi.org/10.1088/0305-4608/13/3/021.

[8] M. Yamamoto, A. Tanaka, R. Fukuda, N. Kondo, T. Nakagawa, Optical control of 4f orbital state in rare-earth metals, Sci. Adv. 11 (2025) 1–10, https://doi.org/10.1126/sciadv.adk9522, eadk9522.

[9] S. Yang, C. Zhou, X. Zhao, F. Liu, Y. Li, H. Chen, L. Ren, J. Xu, X. Zhang, Y. Fang, T. Zhang, Advancements and prospects of near-infrared-light driven $CO_2$ reduction reaction, Chem. Soc. Rev. 54 (15) (2025) 7174–7215, https://doi.org/10.1039/D4CS00721B.

[10] J. Liao, M. Zhang, C. Wang, H. Zhou, L. Xu, F. Tang, X. Li, Tunable oxygen vacancies enable dynamic infrared response for efficient $CO_2$ reduction on plasmonic BiOx, ChemSusChem 18 (2025) e202501050, https://doi.org/10.1002/cssc.202501050.

[11] A. Sanchez-Oliva, J. Fernández-Cestau, L. Garcia, R. Carrillo, M.I. Garcia-Tecedor, Near-infrared emissive optical waveguides and photophysical insights based on 5H-[1,2,5]thiadiazolo[3,4-f]benzotriazole (BTD-BTZ), Dyes Pigments 242 (2025) 112949, https://doi.org/10.1016/j.dyepig.2025.112949.

[12] J. Chen, Y. Xu, P. Zhao, L. Peng, X. Liu, Identifying lanthanide energy levels in semiconductor nanoparticles enables tailored multicolor emission through rational dopant combinations, Acc. Chem. Res. 58 (2025) 1473–1483. ⟨https://pubs.acs.org/doi/full/10.1021/acs.accounts.5c00116⟩.

[13] Y. Pu, J. Zhang, Y. Zhang, Q. Sun, C. Zhu, Interfacial molecular engineering of rare earth-doped nanocrystals: basic principles, construction strategies, and advanced applications, Laser Photon, Rev 19 (2025) 2500156. ⟨https://onlinelibrary.wiley.com/doi/abs/10.1002/lpor.202500156⟩.

[14] J.M. Bennett, Rare earth mineral flotation – a comparison of silicates to oxides, carbonates and phosphates (Ph.D. Dissertation), ProQuest, 2025, ⟨https://www.proquest.com/openview/bea0850f4b7c977fb1e2db5993a12817/⟩ (Ph.D. Dissertation).

[15] A.M. Enad, J.M. Rzaij, Study on the structural and optical properties of CuO thin films mixed with $La_2O_3$ deposited using pulsed laser deposition for future optoelectronic and gas sensing devices applications, Samarra J. Pure Appl. Sci. 7 (2) (2025) 185–198, https://doi.org/10.54153/sjpas.2025.v7i2.1123.

[16] A. Khallouqi, H. Sekkat, O. El Rhazouani, A. Halimi, Phy-X/PSD and Gate/Geant4 analysis of gamma-ray shielding in novel tellurite-based glasses, Ceram. Int. 51 (6) (2025) 8168–8177, https://doi.org/10.1016/j.ceramint.2024.12.252.

[17] Y. Shi, T. Wang, R. Zhang, M. Xu, J. Liu, Harnessing photo-energy conversion in nanomaterials for precision theranostics, Adv. Mater. 37 (2025) e202501623, https://doi.org/10.1002/adma.202501623.

[18] R.R. Ghosh, P. Singh, M. Banerjee, Structural studies and physical properties of $Gd_2O_3$-doped borate glass, J. Mater. Sci. Mater. Electron 32 (2021) 16340–16350, https://doi.org/10.1007/s10854-021-06022-1.

[19] M. Ajmal, A.M. Khan, M.A. Khan, M. Siddique, M.R. Khan, M. Imran, Structural and optical properties of $La_2O_3$:$Ho^{3+}$ and $La(OH)_3$:$Ho^{3+}$ crystalline particles, Mater. Today Proc. 4 (3C) (2017) 4900–4905, https://doi.org/10.1016/j.matpr.2017.04.093.

[20] R.K. Yadav, S. Patel, M.K. Singh, A. Das, A comparison of photocatalytic degradation of six organic dyes by pH-modulated $La_2O_3$ nanoparticles, J. Mater. Sci. Mater. Electron. 36 (2025) 1051, https://doi.org/10.1007/s10854-025-15064-8.

[21] T. Honma, Y. Benino, T. Fujiwara, T. Komatsu, R. Sato, V. Dimitrov, Electronic polarizability, optical basicity, and interaction parameter of $La_2O_3$ and related glasses, J. Appl. Phys. 91 (2002) 2942–2950, https://doi.org/10.1063/1.1436292.

[22] M. Safari-Amiri, S. Mortazavi-Derazkola, M. Salavati-Niasari, S.M. Ghoreishi, Synthesis and characterization of $Dy_2O_3$ nanostructures: enhanced photocatalytic degradation of rhodamine B under UV irradiation, J. Mater. Sci. Mater. Electron 28 (9) (2017) 6467–6474, https://doi.org/10.1007/s10854-017-6333-8.

[23] A. Abdallah, C. Bouzidi, Optical studies of $Dy_2O_3$ doped phosphate glasses for potential white luminescence applications, Solid State Sci. 165 (2025) 107958, https://doi.org/10.1016/j.solidstatesciences.2025.107958.

[24] S. Ghosh, S. Kumar, P. Roy, A. Naskar, A. Sharma, D. Das, P. Chakraborty, Bioinspired synthesis of intrinsically radiolabeled $Dy_2O_3$ nanoparticles as an in vivo generator of $^{166}Dy/^{166}Ho$: a smart choice for theranostics engineering, ACS Appl. Mater. Interfaces 17 (30) (2025) 42767–42780, https://doi.org/10.1021/acsami.5c08153.

[25] A. Buasri, A. Boonpanya, A. Yangderm, T. Kensopha, V. Loryuenyong, Microwave synthesis of luminescent recycled glass containing $Dy_2O_3$ and $Sm_2O_3$, J. Compos. Sci. 9 (2) (2025) 64, https://doi.org/10.3390/jcs9020064.

[26] B.N. Swetha, V. Hegde, D.R. Lavanya, M.K. Kokila, Enhanced solid-state lighting performance of AuNPs-embedded $Dy_2O_3$-containing $La_2O_3$-$Na_2O$-$TeO_2$-$B_2O_3$ glasses, Ceram. Int. (2025). ⟨https://www.sciencedirect.com/science/article/pii/S0272884225036806⟩.

[27] M. Kok, K.S. Mohammed, E.O. Oner, I.N. Qader, Y. Aydogdu, Exploring the impact of $Dy_2O_3$ nanoparticles on the physical characteristics of poly(lactic acid) and polyhydroxyalkanoate composites, J. Polym. Res. 32 (1) (2025) 3, https://doi.org/10.1007/s10965-024-04235-6.

[28] M. Ibrahim, Synthesis, stability, and luminescent properties of $NaYF_4$:$Yb^{3+}$,$Er^{3+}$ upconversion rare-earth nanoparticles, University of Central Florida, 2025. ⟨https://stars.library.ucf.edu/etd2024/157/⟩ (accessed Aug. 18, 2025).

[29] K.-L. Lou, J.-W. Bai, Fluorophores used in NIRF imaging, in: G.-J. Zhang, J.-H. Dong, L. Liu, J.-W. Bai (Eds.), Application of Near-infrared Fluorescence Imaging in Cancer Surgery, Springer Nature, Singapore, 2025, pp. 33–63, https://doi.org/10.1007/978-981-96-6875-5_3.

[30] M. Ghassemi, S.R. Abedini, S.T. Khosravi, F. Mahmoudi, P. Soleimani, H.A. Lari, Evaluating the combination and comparison of ablative fractional lasers ($CO_2$, Er:YAG) with pulsed dye laser (PDL) for treating hypertrophic scars: a systematic review, Lasers Med. Sci. 40 (1) (2025) 129, https://doi.org/10.1007/s10103-025-04382-2.

[31] S. Gu, X. Tang, Y. Zhao, Y. Peng, H. Zhang, Generation and dynamics of soliton from GaGeTe quantum dots based erbium-doped fiber lasers, Opt. Laser Technol. 181 (2025) 112027, https://doi.org/10.1016/j.optlastec.2024.112027.

[32] S.N. Nazrin, M.S. Sutrisno, H.B. Zaman, N. Jothi, A. Assaiqeli, S. Ezzine, Enhanced photoluminescence and optical properties of erbium-doped zinc tellurite glasses for visible and near-infrared photonic applications, J. Lumin 281 (2025) 121184, https://doi.org/10.1016/j.jlumin.2025.121184.

[33] Y.-Y. An, X. Liu, J. Li, Z. Zhang, L. Chen, Quantum teleportation from telecom photons to erbium-ion ensembles, Phys. Rev. Lett. 135 (1) (2025) 010804, https://doi.org/10.1103/PhysRevLett.135.010804.

[34] M.M.A. Eid, R.S. Elshaer, A.F. Abdelrahman, A.M. El-Gendy, CWDM communication system based inline erbium-doped fiber amplifiers with the linear geometrical polarization model, J. Opt. Commun. 45 (S1) (2025) S431–S443, https://doi.org/10.1515/joc-2021-0033.

[35] M.A. Patwardhan, S. Khapre, M. Ingale, A.N. Yerpude, MATLAB simulation for optimization of erbium-doped fiber amplifier, J. Opt. (2025), https://doi.org/10.1007/s12596-025-02880-8.

[36] X. Kang, K. Jiang, S. Ge, K. Wei, Y. Zhou, B.B. Xu, K. Wang, K. Wang, Frontier in advanced luminescent biomass nanocomposites for surface anticounterfeiting, ACS Nano 19 (2025) 11547–11575, https://doi.org/10.1021/acsnano.4c17883.

[37] R. Wang, H. Hou, Y. Bai, R. Zeng, Luminescence regulation of rare-earth based double perovskites by doping and applications, J. Lumin 277 (2025) 120990, https://doi.org/10.1016/j.jlumin.2024.120990.

[38] B. Xu, J. Wang, C. Zhang, Y. Li, Luminescence properties related to energy transfer process and cross relaxation process of $Y_2O_3$:$Yb^{3+}$/$Er^{3+}$ thin films doped with $K^+$ ion, Opt. Mater. 118 (2021) 111290, https://doi.org/10.1016/j.optmat.2021.111290.

[39] H. Thabit, H.M. Ariffin, M.A. Mahdi, A.A. Saad, Exploring the properties of $Dy_2O_3$–$Y_2O_3$ co-activated telluro-borate glass: structural, physical, optical, thermal, and mechanical properties, Heliyon 9 (2023) e18309, https://doi.org/10.1016/j.heliyon.2023.e18309.

[40] R. Kaur, V. Bhatia, D. Kumar, S.M.D. Rao, S.P. Singh, A. Kumar, Physical, structural, optical and thermoluminescence behavior of $Dy_2O_3$ doped sodium magnesium borosilicate glasses, Results Phys. 12 (2019) 827–839, https://doi.org/10.1016/j.rinp.2018.12.005.

[41] H. Zhang, J. Li, W. Fang, Q. Sun, Synthesis and luminescence properties of Bi3+ and Re3+ (Re = Eu, Dy, Tm) co-doped $GdVO_4$ phosphors for latent fingerprint detection, J. Phys. Conf. Ser. 2920 (2025) 012002, https://doi.org/10.1088/1742-6596/2920/1/012002/meta.

[42] H.-S. Kim, J.-W. Choi, K.-Y. Park, Synthesis and optical properties of $Dy^{3+}$-doped $Y_2O_3$ nanoparticles, J. Korean Phys. Soc. 60 (2012) 244–249, https://doi.org/10.3938/jkps.60.244.

[43] Y. Hu, B. Xu, W. Li, L. Liang, F. Fei, Q. Lin, Upconversion nanoparticles doped optical lens: let's see the near-infrared light, J. Nanobiotechnol 22 (1) (2024) 332, https://doi.org/10.1186/s12951-024-02564-8.

[44] Y. Geng, X. Zhang, R. Chen, Q. Li, L. Zhao, Challenges and opportunities of upconversion nanoparticles for emerging NIR optoelectronic devices, Adv. Mater.37 (2025) 2419678, https://doi.org/10.1002/adma.202419678.

[45] Y. Yang, H. Li, Z. Liu, F. Wang, Q. Zhang, H. Zhao, Switching the NIR upconversion of nanoparticles for the orthogonal activation of photoacoustic imaging and phototherapy, Nat. Commun. 13 (1) (2022) 3149, https://doi.org/10.1038/s41467-022-30713-w.

[46] K.J. Lee, J. Park, C. Wang, M. Zhao, Near-infrared to visible photon upconversion with gold quantum rods and aqueous photo-driven polymerization, J. Am. Chem. Soc. 147 (2025) 28241–28250. ⟨https://pubs.acs.org/doi/10.1021/jacs.5c08826⟩.

[47] L. Lian, X. Zhang, C. Liu, J. Chen, R. Yang, Efficient dual-band white-light emission with high color rendering from zero-dimensional organic copper iodide, ACS Appl. Mater. Interfaces 13 (19) (2021) 22749–22756, https://doi.org/10.1021/acsami.1c03881.

[48] X. Li, Y. Zhang, P. Chen, R. Liu, T. Wu, Efficient dual broadband VIS–NIR emission in Mo-doped double perovskites enabling detection and imaging applications, Chem. Eng. J. 517 (2025) 164543, https://doi.org/10.1016/j.cej.2025.164543.

[49] H. Wang, Z. Li, J. Zhao, L. Chen, Y. Tang, Dual-band white light emission and temperature-dependent luminescence of $Sn^{2+}$ in the metastable structure of $Cs_2CaCl_4(H_2O)_2$, Inorg. Chem. Front 12 (5) (2025) 1927–1934, https://doi.org/10.1039/D4QI03288H.

[50] J.L. Pardal-Refoyo, B. Pardal-Peláez, Usefulness of autofluorescence detection of the parathyroid glands with PTeye™ system: scope review, medRxiv (2025), https://doi.org/10.1101/2025.02.01.25321520.

[51] Z. Xiao, K. Wang, X. Lu, X. Sun, F. Lu, Fabrication of multimodal optical imaging agents through direct triplet energy transfer from rare-earth doped nanoparticles, J. Lumin 280 (2025) 121092, https://doi.org/10.1016/j.jlumin.2025.121092.

[52] M. Yang, X. Zhang, Advances in near infrared optoelectronics material selection, structure design and performance analysis, Front. Phys. 11 (2023) 1291695, https://doi.org/10.3389/fphy.2023.1291695.

[53] A. Sood, SiGe-based visible–NIR photodetector technology for optoelectronic applications. in: Advanced Optoelectronic Materials and Devices, IntechOpen, 2015, pp. 315–361, https://doi.org/10.5772/58517.

[54] J. Rosowska, L. Kowalska, M. Gorski, R. Winiarski, Growth of ZnO nanoparticles using microwave hydrothermal method—search for defect-free particles, Nanomaterials 15 (3) (2025) 230, https://doi.org/10.3390/nano15030230.

[55] N. Prasad, R. Banerjee, M. Dutta, A. Sharma, Highly selective photocatalytic degradation of organic pollutants by ZnO@C core–shell nanoparticles via superoxide radical pathway, ChemRxiv Prepr. (2025). ⟨https://chemrxiv.org/engage/chemrxiv/articledetails/688096cd728bf9025ec8fac6⟩.

[56] R. Varghese, S.M. Jose, J.K. Thomas, S.C. Babu, Fe-doping induced optical, electrical, and dielectric property enhancement in strontium titanate, J. Mater. Sci. Mater. Electron 36 (23) (2025) 1428, https://doi.org/10.1007/s10854-025-15508-1.

[57] A.N. Kumar, M. Balakrishna, U. Desai, R. Rakshith, K.M. Ambika, P. Soumya, C. R. Ravikumar, S. Senthil Vadivu, N. Naik, Solution combustion synthesis of ZnO doped CuO nanocomposite for photocatalytic and sensor applications, Sci. Rep. 15 (2024) 338. https://www.nature.com/articles/s41598-024-82764-2.

[58] M. Anwar, T. Hussain, F.N. Khan, S. Javed, H. Rafiq, Solution-combustion synthesis of $AgCo_3O_4$/FeMn–O multiphase composite for high-performance asymmetric supercapacitor, J. Energy Storage 105 (2025) 114602, https://doi.org/10.1016/j.est.2024.114602.

[59] M.S. Eraky, S.S. Elsherif, M.M.S. Sanad, Recent trends in upconversion luminescent inorganic materials and nanomaterials for enhanced photovoltaic solar cell and biological applications, J. Fluor. (2025) 1–25, https://doi.org/10.1007/s10895-025-03462-1.

[60] S. Sood, R. Sharma, P. Gupta, V.K. Singh, Enhancing optoelectronic performance through rare-earth-doped ZnO: insights and applications, Photonics 12 (5) (2025) 945, https://doi.org/10.3390/photonics12050945.

[61] S. Geng, X. Zhang, Q. Li, R. Chen, Y. Zhao, Challenges and opportunities of upconversion nanoparticles for emerging NIR optoelectronic devices, Adv. Mater. 37 (2025) 2419678, https://doi.org/10.1002/adma.202419678.

[62] A. Buasri, A. Boonpanya, A. Yangderm, T. Kensopha, V. Loryuenyong, Microwave synthesis of luminescent recycled glass containing $Dy_2O_3$ and $Sm_2O_3$, J. Compos. Sci. 9 (2) (2025) 64, https://doi.org/10.3390/jcs9020064.

[63] V. Jaiswal, R. Patel, A. Mehta, S. Sharma, Trap depth analysis of $Dy^{3+}$-doped strontium halophosphate phosphor for thermoluminescence dosimetry applications, J. Lumin (2025), https://doi.org/10.1016/j.jlumin.2025.121500.

[64] N. Edayadulla, C.S. Sundari, Role of stabilizing agent in nanomaterials. Sustainable Green Synthesised Nano-Dimensional Materials for Energy and Environmental Applications, CRC Press, Boca Raton, 2024, pp. 47–63, https://doi.org/10.1201/9781003337241-3.

[65] A.-C. Bijlard, F.R. Wurm, K. Landfester, Functional colloidal stabilization, Adv. Mater. Interfaces 4 (1) (2017) 1600443, https://doi.org/10.1002/admi.201600443.

[66] L. Xu, J. Zhao, M. Xu, H. Li, Stability and reactivity: positive and negative aspects for nanoparticle processing, Chem. Rev. 118 (7) (2018) 3209–3250, https://doi.org/10.1021/acs.chemrev.7b00769.

[67] K. Gopal, S. D. V, M. Ranot, Surface-engineered $Dy_2O_3$ nanoparticles: a comparative study of pure and PVP-coated $Dy_2O_3$ nanoparticle variants for high-fidelity photoluminescence, latent fingerprinting, anti-counterfeiting and solid-state lighting applications, Surf. Interfaces 69 (2025) 106741, https://doi.org/10.1016/j.surfin.2025.106741.

[68] O. Portillo, M.C. Portillo, H. Santiesteban, L. Serrano, J. Alvarado, Y. Reynoso, Green chemistry synthesis and structural and optical study of $Dy_2(CO_3)_3 \rightarrow Dy_2O_3$ transition, Rev. Mex. Fis. 69 (2023) 021302, https://doi.org/10.31349/RevMexFis.69.021302.

[69] T. Wang, R. Zhang, Z. Li, M. Chen, S. Liu, Large enhancement of properties in strained lead-free multiferroic solid solutions with strong deviation from Vegard's law, Matter 8 (1) (2025) 101874, https://doi.org/10.1016/j.matt.2024.09.018.

[70] N.M. Ibrahim, O.A. Fouad, A.S. Eliwa, G.G. Mohamed, W.M. Hosny, M. A. Hefnawy, Chemical and green synthesis of silver nanoparticles and their use as an electrocatalyst for water splitting, Int. J. Hydrog. Energy 159 (2025) 150536, https://doi.org/10.1016/j.ijhydene.2025.150536.

[71] C. Quan, Y. Zhao, J. Liu, F. Yang, M. Huang, Crystal structure and thermal and mid-infrared broadband luminescence characteristics of a novel Er,Dy:YAP crystal, CrystEngComm 27 (18) (2025) 2937–2943, https://doi.org/10.1039/D5CE00170F.

[72] M. Lobet, F. Gillissen, N. De Moor, J. Dewalque, P. Colson, R. Cloots, A. Maho, L. Henrard, Plasmonic properties of doped metal oxides investigated through the Kubelka–Munk formalism, ACS Appl. Opt. Mater. 3 (2) (2025) 456–468, https://doi.org/10.1021/acsaom.4c00432.

[73] P.R. Jubu, O. Adedokun, C. Mbakaan, A. Nathan-Abutu, E. Danladi, J.N. Tsaviv, P.I. Kyesmen, B.J. Akeredolu, Accuracy in estimating the absorption coefficient of powdered nanomaterials: resolving misconceptions in Tauc plot application for energy bandgap determination, J. Mater. Sci. Mater. Electron 36 (2025) 15037, https://doi.org/10.1007/s10854-025-15037-x.

[74] S. Lee, Q. Wang, V. Chakrapani, Interplay of surface transfer doping and Burstein–Moss shift: implications for band gap, doping, and catalysis, Phys. Rev. Mater. 9 (8) (2025) 085801, https://doi.org/10.1103/rzvg-r25y.

[75] T.K. Sarangi, R. Panda, B. Kishan, K.K. Naik, Octylamine-mediated growth of europium-doped silver selenide nanoparticles as a superior electrode material for electrochemical applications, RSC Adv. 15 (2025) 3245–3254, https://doi.org/10.1039/D5RA03245H.

[76] D. Barreca, A. Gasparotto, A. Milanov, E. Tondello, A. Devi, R.A. Fischer, Nanostructured $Dy_2O_3$ films: an XPS investigation, Surf. Sci. Spectra 14 (1) (2007) 52–59, https://doi.org/10.1116/11.20080702.

[77] L.E. Khatib, A.M. Abdallah, M. Noun, N.E. Ghouch, G.O. Younes, R. Awad, Synthesis and magnetic properties of PVP capped $Ni_{0.6}Zn_{0.2}Sb_{0.2}Fe_2O_4$ nanoferrites, Appl. Phys. A 131 (6) (2025) 499, https://doi.org/10.1007/s00339-025-07629-1.

[78] R.N. Bharathi, T. Ramachandran, G. Rekha, Cu-doping-induced modulation of crystal structure and magnetic anisotropy in $Dy_3Cu_xFe_{5-x}O_{12}$ garnet nanocrystals, Appl. Phys. A 129 (2023) 481, https://doi.org/10.1007/s00339-023-06753-4.

[79] S. Chanda, R. Maity, S. Saha, A. Dutta, T.P. Sinha, Double perovskite nanostructured $Dy_2CoMnO_6$: an efficient visible-light photocatalyst: synthesis and characterization, J. Sol. Gel Sci. Technol. 99 (2021) 600–613, https://doi.org/10.1007/s10971-021-05605-y.

[80] F.A. López, M.E. Escudero, F.J. Alguacil, I. Llorente, A. Urbieta, P. Fernández, F.A. López, Dysprosium removal from water using active carbons obtained from spent coffee ground, Preprints (2019). https://doi.org/10.20944/preprints201908.0076.v1.

[81] G. Wang, D. Liu, S. Fan, Z. Li, J. Su, High-k erbium oxide film prepared by sol–gel method for low-voltage thin-film transistor, Nanotechnology 32 (2021) 215202, https://doi.org/10.1088/1361-6528/abe439.

[82] I.A. Safo, C. Dosche, M. Özaslan, Effects of capping agents on the oxygen reduction reaction activity and shape stability of Pt nanocubes, ChemPhysChem 20 (2019) 3010–3023, https://doi.org/10.1002/cphc.201900653.

[83] J. Xian, Q. Hua, Z. Jiang, Y. Ma, W. Huang, Size-dependent interaction of the poly (N-vinyl-2-pyrrolidone) capping ligand with Pd nanocrystals, Langmuir 28 (17) (2012) 6736–6741, https://doi.org/10.1021/la300786w.

[84] Effect of PVP molecular weights on the synthesis of ultrasmall CuS nanoflakes: synthesis, properties, and potential application for phototheranostics, ACS Appl. Bio Mater. 7 (2024) 1671–1681.

[85] M. Hussain, M. Kalulu, Z. Ahmad, O. Ejeromedoghene, G. Fu, Rapid fabrication of polyoxometalate-enhanced photoresponsive films from ethyl cellulose (EC) and polyvinylpyrrolidone (PVP), Int. J. Biol. Macromol. 280 (2024) 136051, https://doi.org/10.1016/j.ijbiomac.2024.136051.

[86] Y. Wu, Z. Liu, R. Chen, S. Hu, The shape evolution of gold seeds and gold@silver core–shell nanostructures, Nanotechnology 20 (30) (2009) 305602, https://doi.org/10.1088/0957-4484/20/30/305602.

[87] Non-adiabatic dynamical simulations to the radiative and non-radiative recombinations of the non-fullerene acceptor excited state to optimize its photoluminescence quantum yield, J. Phys. Chem. Lett. 16 (2025) 3359–3365. https://pubs.acs.org/doi/abs/10.1021/acs.jpclett.5c00427.

[88] Y. Yuan, J. Gao, Z. Liu, Controlling of circularly polarized luminescence via modulating the angle between transition electric and magnetic dipole moments, Adv. Funct. Mater. (2025), https://doi.org/10.1002/adfm.202421020.

[89] E.A. Anashkina, A.V. Andrianov, Wavelength-switchable laser and Raman generation in a hybrid fiber–microresonator system, J. Light. Technol. 43 (12) (2025) 5883–5889, https://doi.org/10.1109/JLT.2025.3555491.

[90] L. Hu, Erbium-doped silica fiber and its applications, in: L. Hu (Ed.), Rare Earth Doped Silica Fiber and Its Applications, Springer Nature, Singapore, 2025, pp. 379–454, https://doi.org/10.1007/978-981-96-5306-5_6.

[91] M.A. Patwardhan, S. Khapre, M. Ingale, A.N. Yerpude, MATLAB simulation for optimization of erbium-doped fiber amplifier, J. Opt. (2025), https://doi.org/10.1007/s12596-025-02880-8.

[92] T.P. Jyothi, K. Gopal, D.V. Sunitha, R. Venkatesh, $Gd_2O_3$ nanoarchitectures: orchestrating radiant tales with $Dy^{3+}$, $Eu^{3+}$, $Pr^{3+}$, and $Sm^{3+}$ for cutting-edge photoluminescence and forensic applications, Ceram. Int. 51 (6) (2025) 7946–7963, https://doi.org/10.1016/j.ceramint.2024.12.232.

[93] A.V. Fulari, S.E. Shirsath, Bright and stable tunable blue luminescent pure bromide perovskites via aminosilanised precursor at room temperature, Chem. Eng. J. 525 (2025) 169834, https://doi.org/10.1016/j.cej.2025.169834.

[94] M. Wang, M. Chen, Y. Wang, X.H. Chen, Synthesis and luminescence performance study of $Er^{3+}$-doped $Na_{1.5}La_{1.5}TeO_6$ phosphor, SSRN Prepr. (2025) 5365548, https://doi.org/10.2139/ssrn.5365548.

[95] P. Parida, S. Rout, D. Behera, Co-doping of Mn and Cr in CdTe thin films: tunable white light emission and structural stability, Phys. B Condens. Matter 715 (2025) 417567, https://doi.org/10.1016/j.physb.2025.417567.

[96] R.V. Tikale, A.R. Kadam, S.J. Dhoble, Comprehensive photoluminescence and Judd–Ofelt analysis of $Eu^{3+}$-activated $Sr_4Gd_3Na_3(PO_4)_6F_2$ phosphor: theoretical elucidation from PL spectra for optimized red emission, Opt. Quantum Electron. 57 (2025) 478, https://doi.org/10.1007/s11082-025-08407-6.

[97] L. Han, X. Zhou, J. Guo, H. Liu, Lattice-matched BaClF/$CsPbBr_3$ heterostructure with enhanced and stable cyan emission to overcome blue overshoot and cyan gap of white LEDs, Laser Photon. Rev. 19 (5) (2025) 2401596, https://doi.org/10.1002/lpor.202401596.

[98] C. Xu, F. Zhang, Z. Yuan, J. Qiao, H. Jiang, Dual-emission organic–inorganic hybrids $(2,6\text{-DTP})_2ZnCl_4$·DMF:$Sb^{3+}$ unlocking high-efficiency luminescence and stability for advanced white LEDs, Inorg. Chem. 64 (28) (2025) 14295–14303, https://doi.org/10.1021/acs.inorgchem.5c01423.

[99] S. Zhang, F. Zhao, S. Liu, Z. Song, Q. Liu, An improved method to evaluate trap depth from thermoluminescence, J. Rare Earths 43 (2) (2025) 262–269, https://doi.org/10.1016/j.jre.2024.02.004.

[100] Z. Zou, P. Liu, R. Dou, K. Liu, Y. Wang, L. Song, L. Tong, G. Yin, W. Kang, W. Cai, Y. Zhang, H. Chen, Y. Son, γ-Ray irradiated polyacrylamide networks enable high-performance Li||S pouch cells, Nat. Commun. 16 (2025) 6729, https://www.nature.com/articles/s41467-025-61942-4.

[101] M.U. Khandaker, A. Karim, N. Alam, Thermoluminescence characterization of h-BN powder for neutron dosimetry applications, J. Lumin 286 (2025) 121411, https://doi.org/10.1016/j.jlumin.2025.121411.
[102] D. Sands, The relationship between thermodynamic and Boltzmann entropies: the role of degrees of freedom, J. Phys. Conf. Ser. 2950 (2025) 012011 https://iopscience.iop.org/article/10.1088/1742-6596/2950/1/012011/meta.
[103] Z. Hu, B. Yan, High-performance ultralong room temperature phosphorescence enabled by HOFs for multiple-photoresponsive olanzapine detection and intelligent latent fingerprint identification, Chem. Eng. J. 518 (2025) 164768, https://doi.org/10.1016/j.cej.2025.164768.
[104] Fingerprint analysis and representation in: Handbook of Fingerprint Recognition, in: D. Maltoni, D. Maio, A.K. Jain, S. Prabhakar, D. Maltoni, D. Maio, A.K. Jain, S. Prabhakar (Eds.), Springer, New York, 2003, pp. 83–130, https://doi.org/10.1007/0-387-21587-5_3.
[105] M. Shin, T. Kim, J. Park, A quantitative analysis study on the effects of moisture and light source on FTIR fingerprint image quality, Sensors 25 (4) (2025) 1276, https://doi.org/10.3390/s25041276.
[106] X. Huang, Collagen morphometry exploration in health and disease (Ph.D. Dissertation), Univ. of Toronto, Canada, 2025, ⟨https://hdl.handle.net/1807/123456⟩ (Ph.D. Dissertation).
[107] F.J.R. Meysman, S. Malkin, R. van de Velde, C. Stock, A hierarchical nickel organic framework confers high conductivity over long distances in cable bacteria, bioRxiv (2025), https://doi.org/10.1101/2025.10.15.123456.
[108] I. Ayoub, N. Patel, S. Choudhary, M.D. Rao, Exploring the $Sr_2Ga_2GeO_7$:$Tb^{3+}$ long persistent luminescence phosphor for cutting-edge forensic solutions in latent fingerprint detection and anticounterfeiting applications, Small 21 (13) (2025) 2500285, https://doi.org/10.1002/smll.202500285.
[109] F. Kraus, D. Muller, P. Schlegel, R. Wolf, Proteome landscapes decode organelle vulnerabilities in cortical and dopaminergic-like induced neurons across lysosomal storage disorders, bioRxiv (2025), https://doi.org/10.1101/2025.10.27.123789.
[110] Q. Jin, S. Liu, H. Zhao, L. Wang, Visually invisible multimode anti-counterfeiting based on highly transparent superamphiphobic/superhydrophilic pattern, Nano Today 61 (2025) 102621, https://doi.org/10.1016/j.nantod.2024.102621.
[111] M. Klausen, J. Zhang, Stevens, Designing physical unclonable functions from optically active materials, Adv. Mater. 37 (2025) 2502059.
[112] A. P. J, K. Ghosh, T. Roy, M. Banerjee, Smart anticounterfeiting approach: mineral oil-free offset ink with fluorescent features and audio signal detected using a customized combi-reader, Prog. Org. Coat. 204 (2025) 109237, https://doi.org/10.1016/j.porgcoat.2025.109237.